1-1-2009

The Planetary Nebula Spectrograph elliptical galaxy survey: the dark matter in NGC 4494

N. R. Napolitano
INAF-Observatory of Capodimonte

Aaron J. Romanowsky
San Jose State University, aaron.romanowsky@sjsu.edu

L. Coccato
Max-Planck-Institut für Extraterrestriche Physik

M. Capaccioli
Universit'a Federico II

N. G. Douglas
Kapteyn Astronomical Institute

See next page for additional authors

Recommended Citation

N. R. Napolitano, Aaron J. Romanowsky, L. Coccato, M. Capaccioli, N. G. Douglas, E. Noordermeer, O. Gerhard, M. Arnaboldi, F. De Lorenzi, K. Kuijken, M. R. Merrifield, E. O'Sullivan, A. Cortesi, P. Das, and K. C. Freeman. "The Planetary Nebula Spectrograph elliptical galaxy survey: the dark matter in NGC 4494" *Monthly Notices of the Royal Astronomical Society* (2009): 329-353. https://doi.org/10.1111/j.1365-2966.2008.14053.x

Mon. Not. R. Astron. Soc. **393,** 329–353 (2009) doi:10.1111/j.1365-2966.2008.14053.x

The Planetary Nebula Spectrograph elliptical galaxy survey: the dark matter in NGC 4494

N. R. Napolitano,[1]† A. J. Romanowsky,[2,3] L. Coccato,[4] M. Capaccioli,[5,6]† N. G. Douglas,[7] E. Noordermeer,[8] O. Gerhard,[4] M. Arnaboldi,[9,10] F. De Lorenzi,[4] K. Kuijken,[11] M. R. Merrifield,[8] E. O'Sullivan,[12] A. Cortesi,[8] P. Das[4] and K. C. Freeman[13]

[1]*INAF-Observatory of Capodimonte, Salita Moiariello, 16, 80131, Naples, Italy*
[2]*UCO/Lick Observatory, University of California, Santa Cruz, CA 95064, USA*
[3]*Departamento de Física, Universidad de Concepción, Casilla 160-C, Concepción, Chile*
[4]*Max-Planck-Institut für Extraterrestriche Physik, Giessenbachstrasse, D-85748 Garching b. München, Germany*
[5]*Dipartimento di Scienze Fisiche, Universit'a Federico II, Via Cinthia, 80126, Naples, Italy*
[6]*INAF - VSTceN, Salita Moiariello, 16, 80131, Naples, Italy*
[7]*Kapteyn Astronomical Institute, Postbus 800, 9700 AV Groningen, the Netherlands*
[8]*School of Physics and Astronomy, University of Nottingham, University Park, Nottingham NG7 2RD*
[9]*European Southern Observatory, Karl-Schwarzschild-Strasse 2, D-85748 Garching, Germany*
[10]*INAF, Osservatorio Astronomico di Pino Torinese, I-10025 Pino Torinese, Italy*
[11]*Leiden Observatory, Leiden University, PO Box 9513, 2300RA Leiden, the Netherlands*
[12]*Harvard-Smithsonian Center for Astrophysics, 60 Garden Street, Cambridge, MA 02138, USA*
[13]*Research School of Astronomy & Astrophysics, ANU, Canberra, Australia*

Accepted 2008 September 24. Received 2008 August 25; in original form 2008 June 13

ABSTRACT

We present new Planetary Nebula Spectrograph observations of the ordinary elliptical galaxy NGC 4494, resulting in positions and velocities of 255 planetary nebulae out to seven effective radii (25 kpc). We also present new wide-field surface photometry from MMT/Megacam, and long-slit stellar kinematics from VLT/FORS2. The spatial and kinematical distributions of the planetary nebulae agree with the field stars in the region of overlap. The mean rotation is relatively low, with a possible kinematic axis twist outside $1R_e$. The velocity dispersion profile declines with radius, though not very steeply, down to $\sim$70 km s^{-1} at the last data point.

We have constructed spherical dynamical models of the system, including Jeans analyses with multi-component Λ cold dark matter (CDM) motivated galaxies as well as logarithmic potentials. These models include special attention to orbital anisotropy, which we constrain using fourth-order velocity moments. Given several different sets of modelling methods and assumptions, we find consistent results for the mass profile within the radial range constrained by the data. Some dark matter (DM) is required by the data; our best-fitting solution has a radially anisotropic stellar halo, a plausible stellar mass-to-light ratio and a DM halo with an unexpectedly low central density. We find that this result does not substantially change with a flattened axisymmetric model.

Taken together with other results for galaxy halo masses, we find suggestions for a puzzling pattern wherein most intermediate-luminosity galaxies have very low concentration haloes, while some high-mass ellipticals have very high concentrations. We discuss some possible implications of these results for DM and galaxy formation.

Key words: planetary nebulae: general – galaxies: elliptical and lenticular, cD – galaxies: individual: NGC 4494 – galaxies: kinematics and dynamics – galaxies: structure – dark matter.

1 INTRODUCTION

The idea that some sort of dark matter (DM) dominates the mass of the Universe arose primarily in the 1970s from observations of the outer kinematics of spiral galaxies (Freeman 1970; Ostriker & Peebles 1973; Rubin, Thonnard & Ford 1978; Bosma 1981), and is now well established on cosmological grounds (Hinshaw et al. 2008). As part of the 'concordance' Λ cold dark matter (CDM) model – including CDM and a cosmological constant (Λ) – DM has been invaluable in describing the formation, evolution and stability of cosmic structures.

†E-mail: napolita@na.astro.it (NRN); mc@na.infn.it (MC)

Yet, despite the successes of the concordance model on cosmological scales, on the scales of galaxies and galaxy clusters, several observational discrepancies continue to challenge cosmological complacency. For instance, ΛCDM simulations of the formation of DM haloes predict a steep central cusp (Navarro, Frenk & White 1996; 1997, hereafter NFW; Moore et al. 1999), at variance with many observations of late-type galaxies (de Blok, Bosma & McGaugh 2003; Gentile et al. 2004, 2005; Gilmore et al. 2007; Salucci et al. 2007; Spano et al. 2008; Kuzio de Naray, McGaugh & de Blok 2008). It remains to be seen whether this discrepancy can be traced to observational problems, to oversimplified predictions of DM halo properties (concerning in particular the inclusion of baryonic effects) or to a failure of the ΛCDM paradigm. The default expectation for baryons is that their dissipation would exacerbate the central DM density problem, but it is possible that processes such as feedback in a complete galaxy formation picture would *decrease* the DM densities.

Given the longstanding DM puzzles in late-type galaxies, it is increasingly important to examine the mass content of early-type galaxies (ETGs), i.e. ellipticals and lenticulars. Since these objects are usually free of cold gas and have their stars moving in random directions, their kinematics are more difficult to sample than in disc galaxies and their dynamics harder to model.

The first obstacle comes from observations. Outside $\sim$1–2R_e (where the projected effective radius R_e is that encircling half the total light of the galaxy), the decreasing surface brightness makes kinematics measurements very difficult (e.g. Halliday et al. 2001; Samurović & Danziger 2005; Corsini et al. 2008). DM constraints from this technique are therefore possible for only a fraction of galaxies (e.g. Kronawitter et al. 2000; Gerhard et al. 2001; Thomas et al. 2007).

Globular clusters (GCs) have classically been used as mass tracers in the haloes of 'bright' galaxies, but the kinematical samples in 'ordinary' ETGs (Capaccioli, Caon & D'Onofrio 1992) have so far been too small for strong constraints (e.g. Puzia et al. 2004; Bergond et al. 2006). Similarly, mass studies using X-ray emission are biased towards massive, group or cluster-central galaxies, while ordinary ETGs are much more difficult to probe (see Paolillo et al. 2003; O'Sullivan & Ponman 2004; Humphrey et al. 2006; Pellegrini & Ciotti 2006; Pellegrini et al. 2007).

Hence, it is not surprising that there is no unbiased, systematic survey of the detailed DM properties of ETGs, comparable to what is available for late-types (Persic, Salucci & Stel 1996).

A way forward is offered by planetary nebulae (PNe), which have become established probes of the stellar kinematics in ETG haloes, where their bright 5007 Å [O III] line stands out against the faint galaxy background (e.g. Ciardullo, Jacoby & Dejonghe 1993; Arnaboldi et al. 1996, 1998; Napolitano, Arnaboldi & Capaccioli 2002; Peng, Ford & Freeman 2004). In addition to their use as large-radius mass probes, PNe have the additional advantage of tracing the kinematics of the underlying field stars, and so their orbital properties can be used to constrain the formation history of the bulk of the host galaxies' stars. In the last few years, a novel observational technique of 'counter-dispersed imaging' (Douglas & Taylor 1999) has overtaken the traditional multi-object spectroscopic follow-up of PNe candidates discovered in narrow-band images. This efficient approach to collecting large samples of PN velocities relies on the comparison of pairs of slitless spectroscopic images taken with the dispersing element rotated by 180° between the exposures, and has been successfully implemented with several different variations (Douglas et al. 2000; Méndez et al. 2001; Teodorescu et al. 2005).

The Planetary Nebula Spectrograph (PN.S; Douglas et al. 2002) is the first custom-designed instrument for counter-dispersed imaging. This instrument's two spectrographic cameras, fed by a beam-splitter arrangement at the grating module, operate simultaneously, securing image pairs from the same collimated beam and via the same filter at the same temperature. The PN.S has begun producing large kinematical samples of PNe in a variety of galaxy types (Merrett et al. 2006; Romanowsky et al. 2003, hereafter R+03; Douglas et al. 2007, hereafter D+07; Coccato et al. 2008; Noordermeer et al. 2008). The first results from a small sample of ordinary ellipticals yielded a surprisingly pseudo-Keplerian decline in the observed velocity dispersion profile, more suggestive of galaxies with a constant mass-to-light ratio (M/L) than of DM-dominated systems (Ciardullo et al. 1993; Méndez et al. 2001; R+03; Sluis & Williams 2006; D+07).

These PN observations have sparked several main interpretations. The first is that the data are compatible with ΛCDM expectations (Mamon & Łokas 2005, hereafter MŁ05; Dekel et al. 2005, hereafter D+05; Oñorbe et al. 2007). The second is that the central DM concentrations of many ordinary ETGs are unexpectedly low (Napolitano et al. 2005, hereafter N+05), akin to similar conclusions among late-types (Kassin, de Jong & Weiner 2006; McGaugh et al. 2007). The third is that a modified form of gravity, rather than DM, dominates the outer regions of galaxies (Milgrom & Sanders 2003; Brownstein & Moffat 2006; Tiret et al. 2007).

The issues raised by D+05 in particular (relating to anisotropy, viewing angle and star–PN connections) were explored by R+03 and D+07 in the context of NGC 3379 – the paragon of an ordinary elliptical, with so far the best available kinematical data. They concluded that the ΛCDM-based interpretations were not convincing, although the situation may be less clear under more general dynamical modelling assumptions (De Lorenzi et al. 2008b, hereafter DL+08b). DL+08b explored flattened galaxy models in detail, and found a fairly wide range of mass profiles permitted for NGC 3379. Although they did not directly test ΛCDM-based mass models, they made an a posteriori comparison to the D+05 simulations. They found that the data permitted total mass models comparable to D+05, but that these required stronger radial anisotropy than found in the simulations.

With various efforts underway to elucidate the implications of the data, there also remains the task of producing the observational results for a broad sample of galaxies. Here, we continue towards this goal by presenting new photometric, kinematical and dynamical results from a second galaxy with preliminary results in R+03: NGC 4494.

NGC 4494 is a LINER E1 galaxy located in the Coma I cloud on the periphery of the Virgo cluster, at a distance of 15.8 Mpc and with a total luminosity of $M_B \sim -20.5$, a value close to the L^* characteristic luminosity. These and other global parameters are listed and referenced in Table 1. The stellar component of NGC 4494 is somewhat discy, with a steep central cusp and signification rotation, exhibiting few peculiarities other than central discs of dust ($\sim$100 pc) and kinematically decoupled stars ($\sim$400 pc), which may imply a recent merging episode (Bender, Saglia & Gerhard 1994), hereafter B+94; (Carollo et al. 1997a; Tran et al. 2001; Lauer et al. 2007). X-ray observations reveal very little hot gas in the halo, implying either a recent interaction which has depleted the gas or a very low mass DM halo (O'Sullivan & Ponman 2004; Fukazawa et al. 2006).

Our new study of NGC 4494 follows the pattern of reduction and basic analysis of NGC 3379 in D+07, but goes further in establishing a stronger framework for deriving and interpreting the mass

Table 1. NGC 4494: basic data.

Parameter	Value	Reference
RA (J2000)	$12^{\rm h}\,31^{\rm m}\,24^{\rm s}$	NED[1]
Dec. (J2000)	$+25^\circ 46' 30''$	NED
$v_{\rm sys}$	$1344\,{\rm km\,s^{-1}}$	NED
$(m-M)_0$	31.0 mag	Tonry et al. (2001)[2]
A_B	0.09 mag	Schlegel et al. (1998)
m_V	9.74 ± 0.10 mag	Section 3.1
m_B	10.55 ± 0.10 mag	Section 3.1
M_V	-21.26 ± 0.10 mag	Section 3.1
M_B	-20.5 ± 0.10 mag	Section 3.1
$(B-V)_0$	0.81 mag	G+94
$R_{\rm e}$	48.2 ± 3.0 arcsec	Section 3.1
σ_0	$150\,{\rm km\,s^{-1}}$	HyperLeda[3]
ϵ	0.162 ± 0.001	App. A
a_4	0.16 ± 0.07	App. A
PA	$-0\overset{\circ}{.}9 \pm 0\overset{\circ}{.}3$	App. A

Notes. (1) http://nedwww.ipac.caltech.edu/
(2) corrected by −0.16 mag (see Jensen et al. 2003).
(3) http://leda.univ-lyon1.fr/ (Paturel et al. 2003).

profile. These include the critical aspects of exploiting higher-order velocity information in the data to break the mass-anisotropy degeneracy, and fitting a suite of physically motivated multi-component mass models.

This paper is organized as follows. Section 2 presents a standard reduction of the PN.S observations of NGC 4494. In Section 3, we present the spatial and kinematical properties of the PN system, comparing them to newly acquired long-slit stellar data. We analyse the system's dynamics in Section 4, and put the mass results in context with other galaxies in Section 5. Section 6 summarizes. New surface photometry for NGC 4494 is tabulated in Appendix A, and some technical aspects of the dynamics are described in Appendices B and C.

2 PN.S OBSERVATIONS OF NGC 4494

We present a new set of PN.S data on NGC 4494, starting with a description of the observations and basic data reduction in Section 2.1, and addressing the completeness and possible contamination of the sample in Section 2.2.

2.1 Observations and data reduction

PN.S observations of NGC 4494 were performed during two runs (2002 March and 2003 February–March; Table 2) under a variety of seeing conditions, for a total integration time of ∼14 hours [equivalent to 6.2 h at a constant seeing of full width at half maximum (FWHM) = 1 arcsec, for a given signal-to-noise ratio (S/N) in the final co-added image[1]]. Preliminary results from the 2002 data were presented in R+03.

The systemic velocity of NGC 4494 (see Table 1) was matched with our 'B' narrow-band (FWHM = 31 Å) filter tilted by 6° to achieve a shift of 7.16 Å of its nominal central wavelength $\lambda_{\rm c}$ = 5033.9 Å (see also Douglas et al. 2002 for further details). The instrument position angle was set to 0°, such that the grating dispersed in the north–south direction.

[1] In background-limited observations, S/N $\propto \sqrt{\rm exptime}$ and S/N $\propto {\rm seeing}^{-1}$, so exptime $\propto {\rm seeing}^{-2}$.

Table 2. Log of NGC 4494 PN.S observations.

Date	Integration (h)	Seeing (FWHM)
2002 March 7	1.3	1.9 arcsec
2002 March 8	1.0	1.6 arcsec
2002 March 9	2.8	1.6 arcsec
2002 March 13	0.7	2.1 arcsec
2002 March 14	5.3	1.4 arcsec
2003 February 28	0.5	1.6 arcsec
2003 March 1	0.5	1.6 arcsec
2003 March 2	0.5	1.6 arcsec
2003 March 3	1.2	1.8 arcsec
2003 March 4	0.5	1.0 arcsec

The observations were processed as detailed in section 2 of D+07.[2] An important step in the procedure is identifying PNe in the dispersed images by their point-like emission, since they are spatially and spectrally unresolved objects. Potential sources of contamination are noise, foreground and background continuum objects, and background galaxies with line emission ([O II] at redshift $z \sim 0.35$ or Lyα at $z \sim 3.14$). The latter two categories can often be identified by their extended shape in the images, while noise is rejected by requiring matching detections in both arms. The point-like objects are extracted using the automated software SExtractor (Bertin & Arnouts 1996), with extraction parameters optimized by experimenting on simulated data sets. The automated selection is complemented by an 'eyeball' check on every PN candidate by at least three observers. This check also picks up some PNe missed by SExtractor in certain regions of the image (near star-trails and the galaxy centre).

PN.S observations near galaxy centres are generally hampered by the increasing dominance of the stellar background, and by crowding as a consequence of the central concentration of the PNe themselves. These effects lead to reduced detection completeness, as well as to confusion in assigning PN pairs detected in the left and right arms, and were more significant in NGC 4494 than in NGC 3379 because of a poorer median seeing, higher stellar surface brightness and larger number of PNe in the case of the former (see Fig. 1). Fortunately, the central galactic regions are not of much concern to us, since the power of the PN.S lies in probing the outer parts of galaxies. We must simply keep in mind that the PN-based results inside ∼50 arcsec should be considered unreliable.

After rejecting ∼30 objects for the lack of unanimous approval from the independent observers, we obtain a remarkable full sample of 267 PN candidates (Table 3; the full table is available with the online version of the article). These objects may still include a small number of background line-emitter contaminants and pair mismatches (see Section 2.2). Their spatial distribution is shown in Fig. 2.

2.2 Completeness and contamination

It is important to understand the completeness of our PN sample as a function of radius and magnitude (see Section 3.1). Therefore, we followed the procedure used in D+07 for estimating the fraction of

[2] Data reduction is via a dedicated pipeline written in the IRAF script language (distributed by National Optical Astronomy Observatory, which is operated by AURA, Inc., under contract with the National Science Foundation), with some additional routines written in FORTRAN.

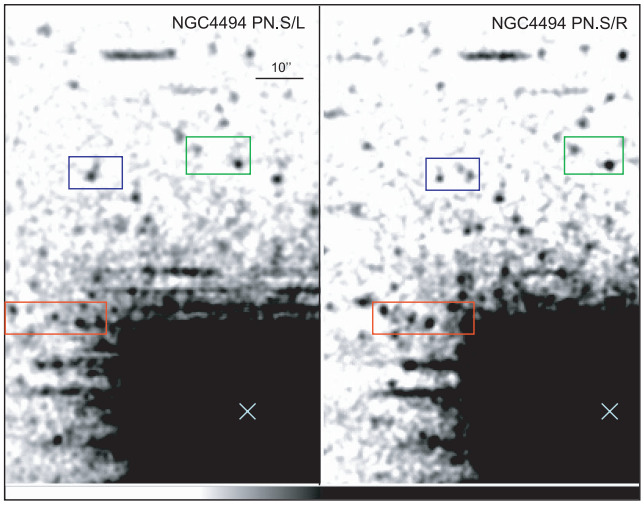

Figure 1. Dispersed images of NGC 4494 from the PN.S, with close-up of the central regions; the 'left' and 'right' camera arm images are marked by PN.S/L and PN.S/R. The galaxy centre is marked by ×. The images have been median subtracted and Gaussian smoothed in order to enhance the emission lines. The stellar background precludes practically any detection for $R < 20$ arcsec, and the crowding is evident. Some sample pair associations are framed: in the green box two pairs clearly separated in the two arms; in the blue box three emissions in the right arm collapse into two in the left arm; in the red box there is a complicated set of four or five emissions.

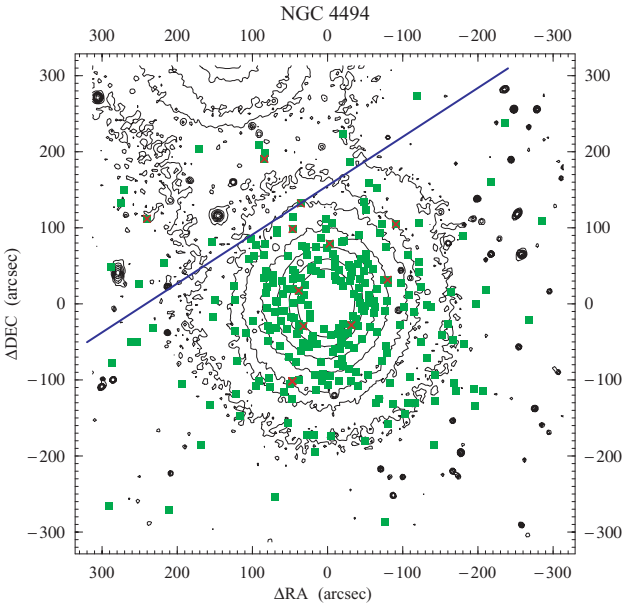

Figure 2. Spatial distribution of objects around NGC 4494. The PNe are marked as filled green boxes, with red × symbols showing objects discarded as phase-space 'outliers' (see text). Surface brightness isophotes from (Megacam g' band) are shown by contours, and the blue solid line marks the boundary where the surface photometry is unaffected by the bright star to the northeast.

Table 3. Catalogue of PNe in NGC 4494. This is a sample of the full catalogue, which is available with the online version of the article (see Supporting Information section).

ID PN.S-EPN-	RA (J2000)	Dec. (J2000)	Wavelength (Å)	$v_{\rm helio}$ (km s^{-1})	J+96
NGC4494-001	12:31:02.70	25:48:11.3	5027.7	1252	-
NGC4494-002	12:31:04.20	25:46:01.4	5029.2	1346	-
NGC4494-003	12:31:06.00	25:50:22.8	5028.7	1313	-
NGC4494-004	12:31:07.50	25:49:04.5	5028.8	1319	-
NGC4494-005	12:31:08.30	25:46:42.9	5029.1	1339	-
NGC4494-006	12:31:08.90	25:44:29.4	5027.1	1217	-
NGC4494-007	12:31:09.30	25:46:24.9	5028.9	1325	-
NGC4494-008	12:31:09.80	25:44:32.7	5030.5	1423	-
NGC4494-009	12:31:09.80	25:44:10.7	5028.6	1309	-
NGC4494-010	12:31:10.40	25:47:54.1	5032.0	1510	-
NGC4494-011	12:31:10.60	25:45:32.1	5029.0	1331	96
NGC4494-012	12:31:11.60	25:44:30.8	5027.8	1262	-
⋮	⋮	⋮	⋮	⋮	⋮

Notes. The PN.S data follow the usual definitions, and the ID is chosen to be compatible with proposed IAU standards (EPN standing for 'Extragalactic Planetary Nebula'). Velocities include the heliocentric correction of 5.7 km s^{-1}.

sources missed by our PN search algorithm. We added to our images a simulated sample of 400 point-like sources randomly placed, with a luminosity function following that expected for the PNe of NGC 4494 and covering a range up to 1 mag fainter than the bright-end cut-off (Ciardullo et al. 1989a) appropriate to this galaxy, $m^* \sim 26.0$ mag (Jacoby, Ciardullo & Harris 1996, hereafter J+06), where the [O III] magnitudes are defined as

$$m_{5007} = -2.5 \log F_{5007} - 13.74$$

(Jacoby 1989). We ran the same SExtractor procedures used for real data, finding that ∼90 per cent of the sources were recovered outside $R \simeq 3R_{\rm e}$ (≃150 arcsec). The detectability decreased to ∼75 per cent at $R \simeq R_{\rm e}$, falling sharply inside this radius. Inside $R \simeq 20$ arcsec, even the brightest (m^*) PNe were not recovered. In the real data, the completeness was higher because of the additional visual checks, so we correct our completeness fraction upwards by using the ratio of automatically and visually recovered PNe in the real data, as a function of radius. This correction is ∼15 and ∼10 per cent in the inner and outer regions. Overall, our 50 per cent completeness limit was $(m^* + 1.2) \sim 27.2$ mag.

We next try to eliminate any residual false PN identifications, which could be due to unresolved background emission-line galaxies, or to PN pair mismatches in crowded regions. As in D+07, we recognize such cases by their apparent 'velocities' which are outlying from the general distribution defined by the bona fide PNe. To this end, we use the 'friendless' algorithm introduced in Merrett et al. (2003) which flags objects deviating by more than $n \times \sigma$ from the velocity distribution of their N nearest neighbours. With $n = 2.5$ and $N = 15$, we find 12 outliers among the NGC 4494 PN candidates (see Fig. 2).

Almost all of the friendless objects are in areas of the field that are either noisy or prone to pair confusion; one or two remaining outliers are probably background galaxies. An alternative approach calculates an azimuthally averaged projected velocity dispersion profile using a moving-window technique, and rejects objects outside the 3σ velocity envelope (see Fig. 3). This approach finds the same outliers as the friendless algorithm, except in the very central regions which are not of importance to our study anyway. The final PN catalogue for NGC 4494 therefore has 255 objects; this is 3.5 times the 73 PNe reported in R+03, with most of the increase coming from a greatly improved method of reducing and stacking the raw data.

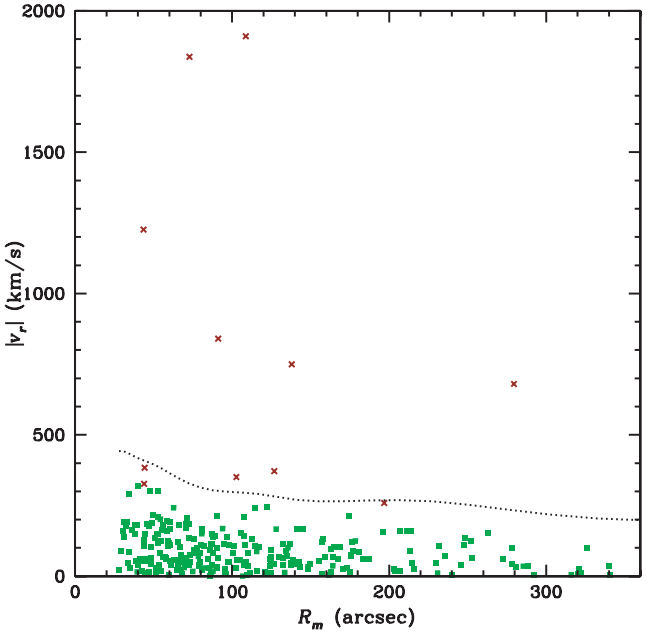

Figure 3. Distribution of line-of-sight velocities of PN candidates around NGC 4494, as a function of radius, and relative to the systemic velocity (1344 km s^{-1}). Red × symbols mark objects designated as outliers by the friendless criterion (one object is off the plot at 108 arcsec, 2518 km s^{-1}), and green boxes show the bona fide PNe. The dotted line shows the 3σ velocity envelope.

We have compared the R+03 preliminary catalogue with our new one and found 70 PNe in common between the two data sets, with no velocity offset between the two samples (for comparison, in D+07 we found an offset of ∼30 km s^{-1} for NGC 3379). The distribution of velocity differences between the R+03 sample, $V_{\rm R+03}$, and the present sample, $V_{\rm PN08}$, $\Delta V = V_{\rm R+03} - V_{\rm PN09}$ is nearly Gaussian (skewness ∼ −0.4 and kurtosis ∼2.9) with a standard deviation of 18 km s^{-1} – which is smaller than the typical instrumental error of the PN.S (20 km s^{-1}; see D+07). We find no systematic trend of velocity difference with spatial position.

We have also cross-checked the J+96 photometric-only catalogue of 183 PN candidates, all of them in our field of view. We recover only 121 of their PNe; of the ones we miss, two-thirds are *not* from the photometrically complete part of their catalogue ($m_{5007} < 27.0$, $R > 1.0$ arcmin). Photometric catalogues are known to be liable to false detections if the off-band images are not deep enough (e.g. Aguerri et al. 2005), and the fraction of the photometric PNe that we have confirmed is consistent with typical recovery rate of photometric candidates in spectroscopic follow-up (e.g. Ciardullo et al. 1993; Arnaboldi et al. 1998) – where the losses can also be due to different factors like astrometric problems, fibre positioning and losses, etc. On the other hand, the vast majority of the objects detected only by the PN.S were below the completeness limit of J+96.

A comparison of spatial positions shows a large average difference in RA and Dec. (∼ −2 and ∼2 arcsec, respectively) between our positions and the ones from J+96. However, the scatter is small (0.6 and 0.5 arcsec, respectively), so there is simply a constant offset between the astrometric systems, which will not compromise the kinematical and dynamical analyses of this paper.

As a final check, we have compared the [O III] magnitudes m_{5007} between the two data sets, finding a scatter of ∼0.4 mag for the whole matched sample, which reduces to ∼0.3 mag for the brightest objects (within 0.3 mag of m^*). Such scatter is consistent with the typical photometric uncertainty of the PN.S, of the order of 0.2–0.3 (see also D+07), once the photometric errors quoted by J+96 are subtracted off in quadrature.

3 PN DISTRIBUTION AND KINEMATICS

We now present the basic properties of the field stars and PNe in NGC 4494, including their distributions in space and velocity. Since an important assumption in strengthening our models is that the PNe are a fair tracer population of the field stars, we compare throughout the properties of the stars and PNe. We examine the spatial distribution in Section 3.1, the rotation field in Section 3.2, the velocity dispersion in Section 3.3 and the kurtosis in Section 3.4.

3.1 Surface photometry and PN spatial distribution

The surface photometry of NGC 4494 available in the literature includes *Hubble Space Telescope* (*HST*) based observations in the *V* and *I* bands (Lauer et al. 2005), and ground-based CCD observations in *BVI* (Goudfrooij et al. 1994, hereafter G+94). As neither study extends far enough in radius to cover the region probed by the PNe (to ∼6 arcmin), new surface photometry was necessary. To this end, we have used imaging data taken on 2006 January 27, with Megacam (McLeod et al. 2000) mounted on the MMT 6.5-m telescope,[3] as part of a programme to image the GC systems of nearby ETGs. A mosaic of 36 2 k × 4 k backside-illuminated CCDs provide a 24 × 24 arcmin field of view with a 0.08 arcsec native pixel scale. Our data consist of 3 × 45 s exposures of NGC 4494 using the Sloan Digital Sky Survey g' filter, read out using 2 × 2 binning, with a pixel scale of 0.16 arcsec. The detailed data reduction and surface photometry analyses are beyond the scope of this paper, but we provide a brief summary here.

The initial data reduction (including overscan, trimming, flat-fielding and bad pixel identification) was performed using the standard routines in the IRAF MSCRED package. World Coordinate System solutions were then found for each exposure by comparison with the Two Micron All Sky Survey catalogue (Jarrett et al. 2003). The images were projected to the tangent plane using SWARP,[4] and stacked in IRAF to create the final corrected images with a seeing-limited resolution of FWHM ∼ 1.4 arcsec. Isophotes from the reduced image are shown in Fig. 2, where it is evident that contamination from a bright star becomes problematic beyond ∼2 arcmin in the northeast direction. Therefore, we have excluded this region as marked in the figure from our surface photometry analysis.

To convert the surface photometry into simple photometric profiles suitable for modelling, we used the IRAF tasks IMSURFIT and ELLIPSE to subtract the background light and fit elliptical isophotes. The resulting profiles of surface brightness, ellipticity and position angle are shown in Fig. 4, mapping from the g' band to the *V* band with an arbitrary normalization required to match the literature data over the radial range of $R = 1.8$–60 arcsec. In this figure, and in general in this paper, the radius used is from the projected intermediate axis R_m, which is related to the major-axis R_a and ellipticity by $R_m \equiv R_a(1 -)^{1/2}$. The data sets are seen to be generally consistent,

[3] The MMT Observatory is a joint facility of the Smithsonian Institution and the University of Arizona.

[4] SWARP is a software developed by Emmanuel Bertin, and it is publicly available at http://terapix.iap.fr/rubrique.php?id_rubrique=49/

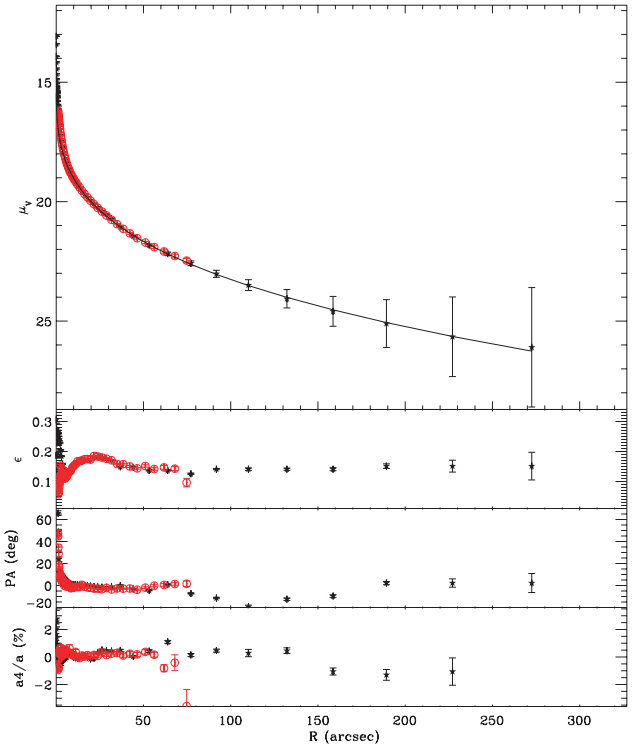

Figure 4. Surface photometry of NGC 4494, as a function of the intermediate-axis radius. Literature data (G+94; Lauer et al. 2005) are shown by red circles, and Megacam data by black stars (this paper), with the uncertainties shown by error bars. Top large panel: composite V-band surface brightness profile. The solid line is the best-fitting Sérsic (1968) formula for $R > 5$ arcsec. Bottom small panels: profiles of ellipticity, position angle and fourth-order isophote shape coefficient a_4, with G+94 data also shown.

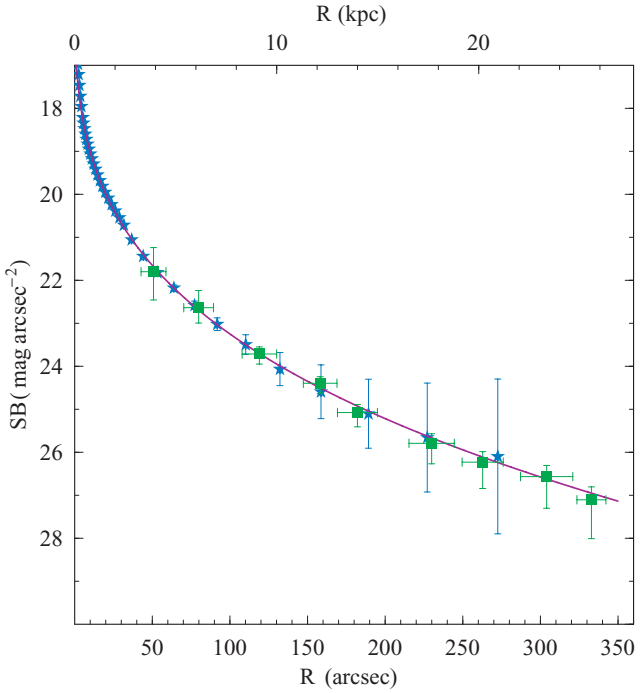

Figure 5. Radial surface density profiles of the field stars (V band; blue star symbols) and of the PNe (green squares) in NGC 4494. The PN number counts have been corrected for spatial incompleteness, and arbitrarily normalized to match the stellar data. The vertical error bars of the PN data in this and in the following figures represent the 1σ uncertainties (based in this case on counting statistics and completeness correction uncertainties), while the horizontal error bars show 68 per cent of the radial range of the PNe in each bin. The purple solid curve is the Sérsic model fit to the stellar photometry (see main text).

except notably inside ∼4 arcsec, where the Megacam data are affected by seeing. We therefore combine the literature and Megacam data into a single V-band surface brightness profile $\mu_V(R)$, listed in Table A1, together with ellipticity and isophote shape parameter a_4 (Bender, Doebereiner & Moellenhoff 1988) values.

In order to make use of the stellar luminosity profile in the dynamical models, we parametrize the surface brightness profile by the Sérsic law:

$$\mu(R) - \mu(0) \propto (R/a_S)^{1/m}, \quad (1)$$

where a_S is a scalelength and m describes the 'curvature' of the profile (Sérsic 1968). Fitting the regions outside the inner disc ($R > 5$ arcsec), we find $a_S = 0.115$ arcsec, $m = 3.30$ and $\mu_0 = 14.82$ mag arcsec^{-2}. These parameters translate into an effective radius of $R_e = 49.5$ arcsec; a more detailed multi-component fit including the central regions yields $R_e = 48.2 \pm 3.0$ arcsec, which is similar to other literature estimates (Faber et al. 1989; de Vaucouleurs et al. 1991). The total extinction-corrected luminosity in the V band is 2.64×10^{10} L$_{V,\odot}$, or $M_V = -21.26$; the uncertainties in the outer surface brightness profile yield a (model-dependent) total luminosity uncertainty of ∼5–10 per cent. To estimate the same quantities in the B band, we use the typical de-reddened colour of $(B - V)_0 = 0.81$ from G+94 to find $L_B = 2.37 \times 10^{10}$ L$_{B,\odot}$ and $M_B = -20.45$. These and other global parameters for NGC 4494 are listed in Table 1.

We next compare the spatial density of the PNe with the field stars, using the PN number density complete to $m^* + 1$ (Section 2.2). Given an arbitrary normalization, the PN profile matches the stellar photometry remarkably well (Fig. 5) – as also generally found in a larger sample of galaxies by Coccato et al. (2008). Therefore, we do not see a pattern emerging to support the scenario proposed by D+05, wherein the observed PNe trace a young stellar subpopulation generated in a merger, with a steeper spatial density profile than the bulk of the field stars.

The normalization of the PN profile corresponds to a specific density parameter of PNe per unit V-band galaxy luminosity of $\alpha_{V,1.0} = (11.5 \pm 3.0)\ (10^9\,\mathrm{L}_\odot)^{-1}$. This translates to a B-band density of $\alpha_{B,1.0} = (10.3 \pm 2.6)\ (10^9\,\mathrm{L}_\odot)^{-1}$, and over the standard magnitude interval to $m^* + 2.5$, $\alpha_{B,2.5} = (42 \pm 11)\ (10^9\,\mathrm{L}_\odot)^{-1}$, which is consistent with the previous result of J+06: $\alpha_{B,2.5} = (31 \pm 3)\ (10^9\,\mathrm{L}_\odot)^{-1}$ (assuming our adopted extinction and distance). The specific frequency is fairly high compared to other ETGs of similar luminosity (cf. Ciardullo et al. 2005; Buzzoni, Arnaboldi & Corradi 2006). The 20 per cent discrepancy between the Planetary Nebula Luminosity Function (PNLF) and Surface Brightness Fluctuations (SBF) distances to NGC 4494 will be investigated in a future paper on PNLFs.

3.2 Rotation

We now examine kinematical streaming motions in the data, i.e. rotation. Although there are data available in the literature for the stellar kinematics of NGC 4494 (B+94), we have obtained new long-slit data as part of a programme to obtain extended stellar kinematics in ETGs. These data will be presented in detail in a

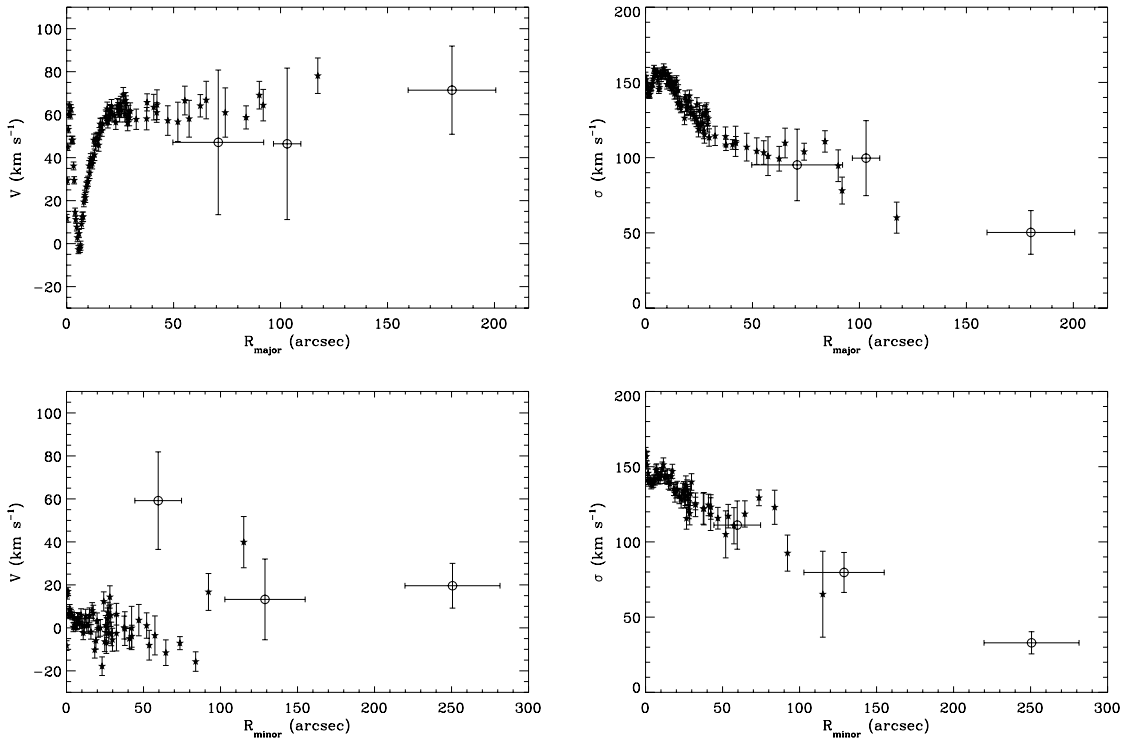

Figure 6. Observed kinematics of stars (filled star symbols) and PNe (open circles) in NGC 4494, with uncertainties shown by vertical error bars. The data from opposite sides of the galaxy have been folded into a single radial axis. The horizontal error bars show 68 per cent of the radial range of each PNe bin. The left-hand panels show the mean velocities relative to the systemic velocity, and the right-hand panels show the dispersions about the mean. The top panels show the major-axis profiles, and the bottom panels show the minor axis.

forthcoming paper (Coccato et al. 2008), and we summarize the main features of the NGC 4494 data here.

Deep spectra were obtained with the European Southern Observatory Very Large Telescope in service mode [Programme ID 076.B-0788(A)] using the FORS2 spectrograph, equipped with the 1400 V grism, through a 1.0 arcsec wide slit. The spectra were taken along the major (PA $= 0^\circ$) and minor (PA $= 90^\circ$) axes of the galaxy, and were re-binned in radius to reach S/N ~ 30 at $R \sim 100$ arcsec $\sim 2\,R_e$. Kinematical stellar templates were chosen from the Indo–US Coudé Feed Spectral Library (Valdes et al. 2004) and convolved with a Gaussian function to match the instrumental FWHM. Various moments of the velocity distribution were extracted using the Penalized Pixel-fitting Method of Cappellari & Emsellem (2004). The fitted spectral range was ∼4560–5860 Å.

The results for the stellar kinematics are shown in Fig. 6. The rotation profile along the major axis shows the kinematically decoupled core inside 5 arcsec, as previously observed by B+94, and coincident with the photometric stellar disc (Carollo et al. 1997a). Since we are interested mostly in the outer kinematics, this very central feature is of no concern for us.

Before examining the PN kinematics, we check their self-consistent systemic velocity by taking the median of the individual PN velocities in the azimuthally complete region of 40–135 arcsec. This value is 1344 km s^{-1}, exactly the same as the NASA/IPAC Extragalactic Database (NED) velocity for NGC 4494.

We then measure the rotation of the PN system by calculating the mean velocity in bins within a wedge of 20° opening angle, aligned with the directions used for the long-slit spectroscopy (PA $= 0^\circ$ for the major axis and PA $= 90^\circ$ for the minor axis). From Fig. 6 (left-hand panels), it is apparent that the rotational properties of the PNe and stars are generally consistent. The discrepancy at small radii (∼50 arcsec) on the minor axis may be caused by the finite width of the PN measurement wedge (i.e. picking up off-axis rotation) and by statistical fluctuations in the velocity sample (see Napolitano et al. 2001).

The constant major-axis rotation velocity of the stars outside the galaxy core of 60 km s^{-1} is found using the PNe to extend to at least $4\,R_e$. The minor-axis rotation is generally small but does suggest some finite rotation at large radii, i.e. a kinematic misalignment. This feature could be caused by a transition in the orbit structure or by projection effects in a smooth triaxial system (e.g. van den Bosch et al. 2008), and may be related to the isophote twisting between ∼75 and ∼200 arcsec (see Fig. 4).

In order to make use of all the PN data rather than just those along the principal axes, we construct 2D maps of the velocity distribution, as in D+07. Assuming at least triaxial symmetry, we produce higher S/N maps by mirroring the PN data points in phase space from (x, y, v) to $(-x, -y, -v)$. We then smooth the velocity field using a median filter and a Gaussian kernel of width $\sigma \sim$ 60 arcsec (∼4.6 kpc) on a regularly spaced grid of 75 arcsec cell widths (see also D+07). The resulting mean velocity field is shown in Fig. 7 (left-hand panel). Again, we see evidence of rotation along the major axis (PA $\sim 0^\circ$) in the galaxy's central parts, twisting to another axis (∼20°) outside $\sim 1R_e$.

We next try an alternative measure of the PN rotation that is insensitive to azimuthal incompleteness. It works by fitting the velocities to a cosinusoidal curve:

$$v(\phi) = v_0 \times \cos(\phi - \phi_0), \quad (2)$$

where ϕ is the position angle of the PNe relative to the major axis (cf. Napolitano et al. 2001). We report the best-fitting parameters for various radial bins in Table 4. Using this technique, there is no

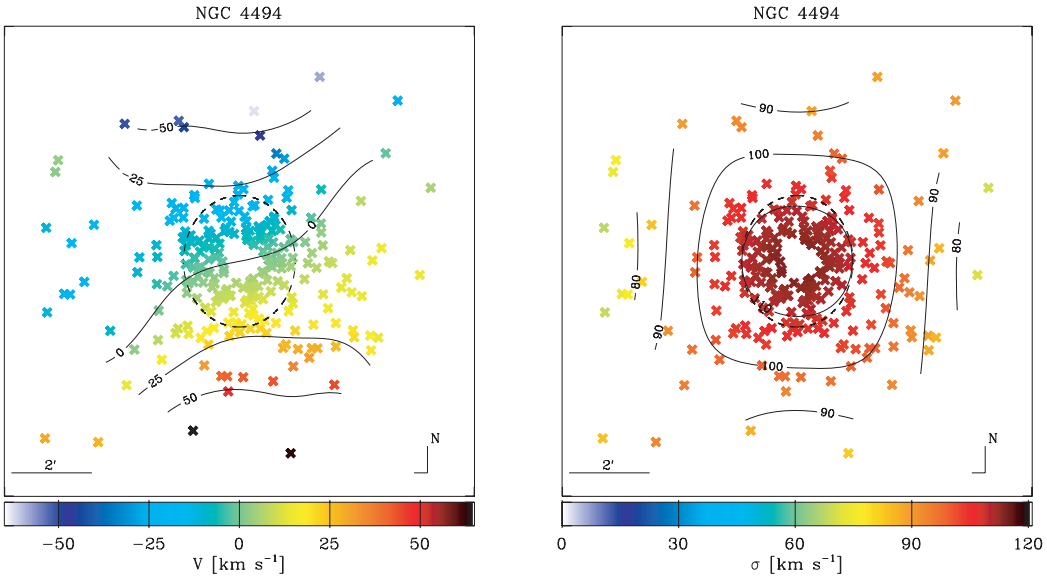

Figure 7. Two-dimensional kinematics of PNe in NGC 4494. Individual PN data points are shown as × symbols, with values given by colours from the scale below. The data set has been doubled by a reflection symmetry, and then smoothed (see main text). Solid curves illustrate iso-velocity contours. The dashed ovals show the 2 R_e isophote. Left-hand panel: mean velocity. Right-hand panel: velocity dispersion about the mean (the squarish contour is partially an artefact of the gridded smoothing technique.).

significant evidence that the rotation is misaligned with the major axis (PA = 0°) at any radius. Although there is a twist at intermediate radii (consistent with the smoothed velocity field in Fig. 7), this is not statistically significant and we will consider the whole sample as consistent with PA = 0° (as in the first row of Table 4).

Finally, we wish to quantify the dynamical significance of rotation within 1 R_e. This is best done with high-quality integral field stellar kinematics data (e.g. SAURON; Cappellari et al. 2007, hereafter C+07), but we can make an estimate based on the available long-slit data. C+07 derived an empirical calibration (their equation 23) between the SAURON rotation dominance parameter within 1R_e and the traditional measure of B+94:

$$\left(\frac{v}{\sigma}\right)_e \approx 0.57 \times \left(\frac{v_{max}}{\sigma_0}\right)_{B+94}, \quad (3)$$

where v_{max} is the maximum observed rotation velocity along the major axis, and σ_0 is the average velocity dispersion within $R_e/2$. Given $v_{max} = 76\,km\,s^{-1}$ and $\sigma_0 = 163\,km\,s^{-1}$ from B+94, we find that $(v/\sigma)_e \approx 0.26$. Comparing this value to the isophote ellipticity from B+94 (= 0.16), we find that NGC 4494 is located firmly in the space occupied by 'fast rotators' (C+07; Fig. 11). Although the calibration above was done for the B+94 data only, very similar results would be obtained using our new photometric and long-slit data.

Table 4. Best-fitting parameters of cosinusoidal rotation model to PN velocity data, in radial bins. ϕ_0 is the direction of maximum velocity.

Radius (arcsec)	N. PNe	v_0 (km s^{-1})	ϕ_0(°)
0–400	255	-23 ± 9	-2 ± 25
0–75	98	-28 ± 18	24 ± 39
75–133	79	-12 ± 16	42 ± 76
133–400	78	-37 ± 14	-8 ± 19

3.3 Velocity dispersion profile

We next examine the random motions in NGC 4494, represented by the velocity dispersion profile. Fig. 6 shows that the PN and stellar dispersions are consistent along the major and minor axes. The dispersion declines steadily with radius, and random motions dominate streaming motions out to ∼100 arcsec (∼2R_e). Fig. 7 (right-hand panel) shows that the dispersion is roughly constant along the galaxy's isophotes.

We reduce these data to a single velocity dispersion profile as a function of the intermediate radius R_m. The rotation and true dispersion profile are folded into a root mean square velocity profile $v_{rms} = \sqrt{v^2 + \sigma^2}$, where v and σ are the rotation and dispersion components, respectively. The rms velocity is a measure of the total kinetic energy, and we henceforth loosely refer to it as the velocity dispersion or VD. We combine the stellar data from the different axes by averaging, while folding the (small) systematic differences into the final uncertainties.[5]

The resulting dispersion data are plotted in Fig. 8. The PN dispersions are similar to those reported in R+03, but are based on 3.5 times as many velocities, and extend to twice the radius. In our subsequent dynamical models, the stellar dispersion will be fitted out to 60 arcsec (∼1 R_e), where it is more accurate, and the PN dispersion outside this radius. To characterize the decline of the dispersion with radius, we fit a power law to the PN data outside 60 arcsec, using a maximum-likelihood method that fits the discrete data with-

[5] The uncertainties in the PN dispersion use a classical analytic formula that assumes a Gaussian distribution, i.e. $\Delta v_{rms} \sim \sqrt{\Sigma_i v_i^2 / 2N^2}$. However, we expect this to produce accurate results in realistic systems (Napolitano et al. 2001), and we have carried out additional Monte Carlo simulations of a simplified galaxy with radial orbits, finding that the dispersion is very accurately recovered with our estimator, with a possible bias to be ∼5 per cent too high. Also, the expression for stellar v_{rms} is valid for comparison with the azimuthally scattered PNe only because we are averaging the major- and minor-axis long-slit data; if only major-axis data were available, the expression would be $v_{rms} = \sqrt{v^2/2 + \sigma^2}$.

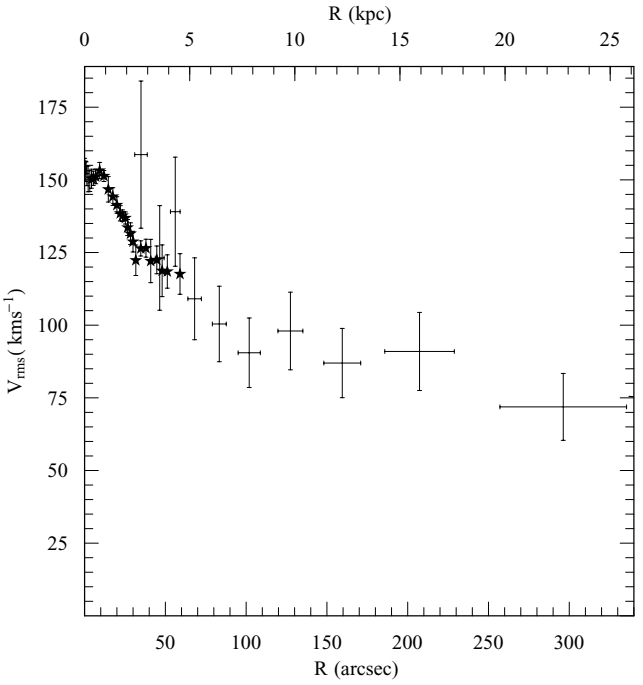

Figure 8. Composite projected velocity dispersion profile of NGC 4494, with data from stars (filled star symbols) and PNe (open circles). The solid curve shows a power-law fit to the PN data outside 60 arcsec.

out binning, though it does assume an underlying Gaussian velocity distribution (Bergond et al. 2006). We find a power-law exponent of -0.2 ± 0.1 (see Fig. 8), which is significantly shallower than -0.6 ± 0.2 found for NGC 3379 (D+07), suggesting a dynamical difference between the two galaxies (discussed further in Section 4).

We also test the sensitivity of the derived velocity dispersion profile to the outliers' selection (Section 2.2). Restoring all the objects to the PN sample which were rejected at $n = 2.5$ but not $n = 5$, we find that the only affected feature is a peak in the dispersion between 100 and 150 arcsec, which does not change the broad trend.

3.4 Higher-order velocity moments

The velocity dispersion is a crude measure of the particle speeds in a collisionless system, whose finer orbital properties can be probed using higher-order moments of the line-of-sight velocity distribution (LOSVD). Stars on isotropic orbits in a galaxy halo with a flat rotation curve have a Gaussian LOSVD (Gerhard 1993). In a tangentially anisotropic system where the particles follow nearly circular orbits, the observed velocities tend to pile up at the circular speed, producing a LOSVD which is flatter than a Gaussian, or even double-peaked. Radial orbits produce centrally peaked LOSVDs with long tails. In the case of integrated-light stellar velocities with fairly high S/N, these LOSVD shapes are described via the Gauss–Hermite moments such as h_4 (Gerhard 1993; van der Marel & Franx 1993). In the case of discrete velocities, it is more straightforward to compute the classical dimensionless kurtosis, $\kappa \equiv \overline{v^4}/(\overline{v^2})^2 - 3$ (see Joanes & Gill 1998 for exact expression and uncertainties[6]).

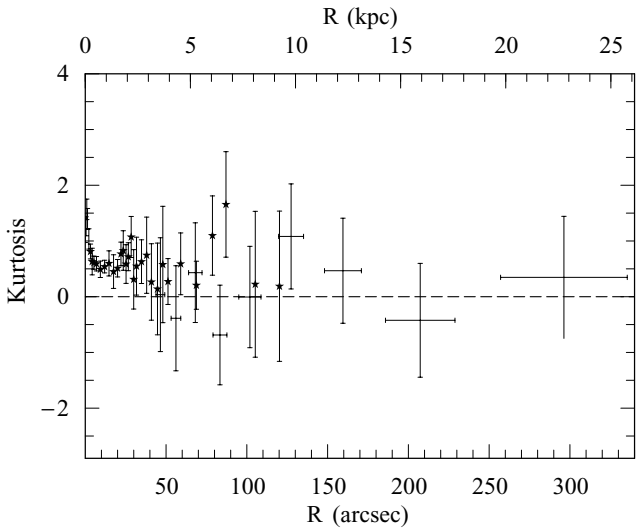

Figure 9. Projected kurtosis profile of NGC 4494, with symbols as in Fig. 8.

Broadly speaking, $\kappa \simeq 0$ for isotropic orbits, $\kappa < 0$ for tangential orbits and $\kappa > 0$ for radial orbits.

We quantify the shapes of the stellar and PN LOSVDs in NGC 4494 in Fig. 9, using the approximate relation $\kappa \simeq 8\sqrt{6}h_4$ for the stars (van der Marel & Franx 1993). The PN kurtosis is fairly noisy, but is consistent with the stellar properties in the region of overlap. However, there is a systematic offset between our stellar h_4 values and those reported by B+94 inside 20 arcsec, where we believe our improved template library procedures yield more reliable results. In the halo, the PN kurtosis is consistent with zero.

4 DYNAMICAL MODELS

We now combine the photometric and kinematical data for the stars and PNe in NGC 4494 into integrated dynamical models in order to derive the mass profile of the galaxy, and test whether or not it hosts a DM halo as expected from ΛCDM. In Section 4.1, we begin with the simple pseudo-inversion mass model[7] used in R+03 and D+07, and introduce a new series of physically motivated kurtosis-based models in Section 4.2. We address systematic issues in Section 4.3.

In both of our main modelling exercises (Sections 4.1 and 4.2), we will apply the spherical Jeans equations to NGC 4494, since the observed stellar isophotes are very round (see Section 3.1 for photometry, and D+07, section 8.1, for discussion of the spherical approximation). We will examine a non-spherical model in Section 4.3 and Appendix C. Given the consistent agreement seen in Section 3 between the stellar and PN properties, we will assume that all of these data are drawn from the same underlying dynamical tracer population. We will also in general omit the stellar kinematics data inside 10 arcsec from our model fits, since there appears to be a strong dynamical change in this nuclear disc region which our smooth Jeans models are not designed to reproduce.

[6] Again, the uncertainty calculation assumes a Gaussian distribution, while for a more general distribution the errors are formally infinite. However, the Monte Carlo simulations mentioned in Section 3.3 demonstrate accurate recovery of the kurtosis using our estimator, with a systematic deviation of no more than ∼0.1.

[7] This is a phenomenological mass inversion method where we reconstruct the mass distribution from the velocity dispersion data. As shown in Section 4.1, since we make use of a parametrized model for the σ_r and the anisotropy parameter in the radial Jeans equation, this is not a full inversion method.

4.1 Pseudo-inversion mass model

Our first series of models uses simple assumptions to convert the observed kinematics into a mass profile $M(r)$. This phenomenological approach, as introduced in R+03 and D+07, is computationally light, need not involve Abel inversion integrals and has no prejudice about the form that $M(r)$ should take, nor about the stellar M/L value (which will be discussed later in this section). On the other hand, it is not possible to directly test any theoretical predictions for the DM distribution, and the resulting mass profile may not even be physical.

The mass modelling procedure consists of five steps.

(i) Adopt a simple smooth parametric function for the intrinsic radial velocity dispersion profile:

$$\sigma_r(r) = \sigma_0 \left[1 + \left(\frac{r}{r_0}\right)^{\eta}\right]^{-1}, \quad (4)$$

where σ_0, r_0, η are a minimalistic set of free parameters.

(ii) Assume a fixed anisotropy profile:

$$\beta(r) \equiv 1 - \sigma_\theta^2/\sigma_r^2, \quad (5)$$

where σ_θ and σ_r are the tangential and radial components of the velocity dispersion ellipsoid, expressed in spherical coordinates.[8]

(iii) Project the radial component of the spatial velocity dispersion σ_r (see equation B4) for comparison with the line-of-sight velocity dispersion data $\sigma_{\rm los}(R)$.

(iv) Iteratively adjust the free parameters in equation (4), to best fit the model to the observed dispersion profile.

(v) Use the best-fitting model (equation 4) in the Jeans equation (4–55) of Binney & Tremaine (1987) to calculate $M(r)$:

$$M(r) = -\frac{\sigma_r^2\, r}{G}\left(\frac{{\rm d}\ln j_*}{{\rm d}\ln r} + \frac{{\rm d}\ln \sigma_r^2}{{\rm d}\ln r} + 2\beta\right), \quad (6)$$

where $j_*(r)$ is the spatial density of the PNe, and corresponds to an Abel deprojection of a smoothed density law fitted to the stellar data. Additional quantities may then be computed, such as the cumulative M/L.

Starting with the minimalist assumption of an isotropic galaxy ($\beta = 0$), we find that the simple model (4) is able to fit the dispersion data very well (Fig. 10). The resulting M/L profile increases clearly with the radius (Fig. 11), providing a strong indication for the presence of an extended DM halo. Using $5\,R_{\rm e}$ (241 arcsec) as a benchmark value, we find that the B-band M/L within this radius is $\Upsilon_{5,B} = 6.3^{+0.6}_{-0.7}\Upsilon_{\odot,B}$, where quoted errors account for the 1σ confidence region in the parameter space (σ_0, r_0, η) of the dynamical model. As we will see in Section 4.2, the derived value for Υ_5 is sensitive to assumptions about $\beta(r)$ but not about the detailed form for $M(r)$, and so is useful as a robust quantity for comparison to theory.

[8] Since we are folding the observed rotational and pressure support into a single parameter $v_{\rm rms}$, we use a similar approach in the Jeans equations, so that technically $\beta(r) \equiv 1 - (\sigma_\theta^2 + \overline{v_\theta^2})/(2\sigma_r^2)$. We thus assume that $\overline{v_\theta^2} = \overline{v_\phi^2}$ everywhere, in contrast to an alternative assumption that $\sigma_\theta^2 = \sigma_\phi^2$, with the rotation support modelled separately (e.g. Hui et al. 1995). Strictly speaking, a spherical model is not warranted for a rotating system anyway, but in the limit of weak rotation, it is a matter of adopting a convenient dynamical approximation. The rotational contribution does rise in the outer parts of NGC 4494 to as high as $v/\sigma \sim 1.4$, potentially causing systematic issues in our mass analysis which would require a more generalized study to quantify.

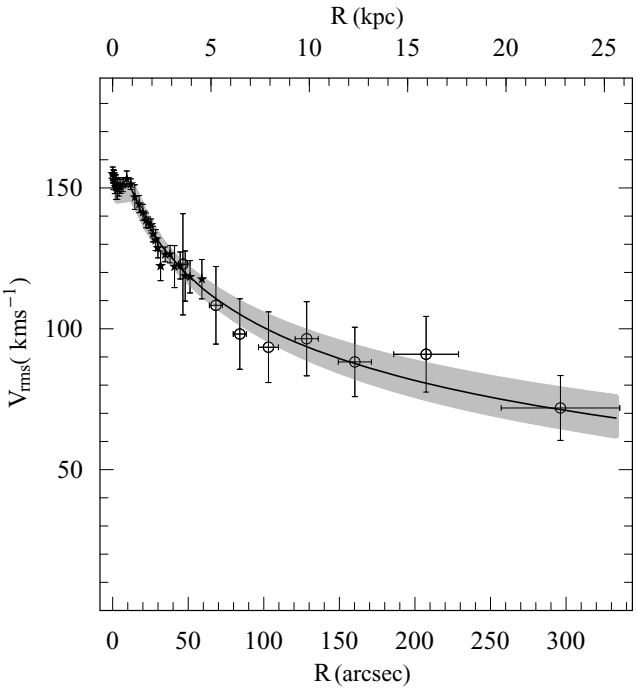

Figure 10. Model fit to the NGC 4494 velocity dispersion data using the pseudo-inversion mass model and assuming isotropy. The best fit and 1σ range of uncertainty are shown by the solid curve and shaded region, respectively.

The shaded regions in Figs 10 and 11 show the statistical modelling uncertainty, but there remains the *systematic* uncertainty implied by the anisotropy in Step (ii) of the procedure. Adopting constant values of $\beta = \pm\,0.5$ for a plausible (though not exhaustive) range of the stellar anisotropy, we can find fits to the data just as good as in Fig. 10. However, the famous mass-anisotropy degeneracy implies very different $M(r)$ profiles, as shown in Fig. 11. Assuming $\beta = +0.5$ implies more DM than with $\beta = 0$, while $\beta = -0.5$ implies a smaller but *non-zero* amount of DM (i.e. a constant M/L is excluded at the 1σ level). Note though that the kurtosis values found in Section 3.4 suggest $\beta \gtrsim 0$, and thus that the higher-mass solutions are to be preferred (as will be explored in the next section).

As a final refinement, we wish to test an anisotropy profile based on theoretical expectations. In general, collisionless systems such as galaxy haloes and clusters that were formed through mergers should have some degree of radial anisotropy (e.g. Diaferio 1999; Colín, Klypin & Kravtsov 2000; Rasia, Tormen & Moscardini 2004; Wojtak et al. 2005; Abadi, Navarro & Steinmetz 2006) – a prediction that has found empirical support from the Galactic halo and from elliptical galaxies (Chiba & Beers 2000; Gerhard et al. 2001; DL+08a,b). In particular, MŁ05 have introduced a radially varying anisotropy profile,

$$\beta(r) = \beta_0 \frac{r}{r + r_{\rm a}}, \quad (7)$$

finding $\beta_0 \simeq 0.5$ and $r_{\rm a} \simeq 1.4\ R_{\rm e}$ when applied to the merger simulations of D+05. Adopting this profile with $r_{\rm a} = 65$ arcsec, we find a M/L profile that is slightly shallower than the pure $\beta = +0.5$ model (Fig. 11).

The overall plausible range for the benchmark-radius M/L of NGC 4494 is $\Upsilon_{5,B} = 5.0$–$9.1\Upsilon_{\odot,B}$ (including both statistical and assumed systematic β uncertainties). This result is very similar to

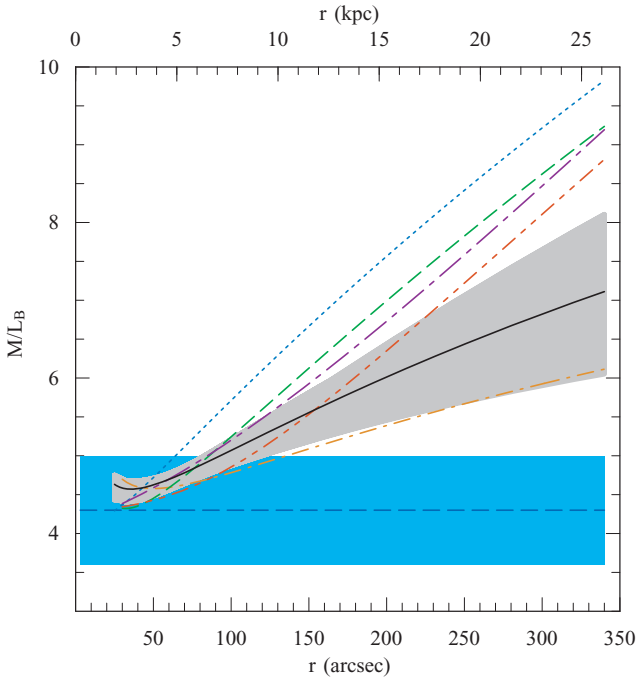

Figure 11. Cumulative *B*-band *M*/*L* of NGC 4494. Most of the curves show results from the mass-inversion method: the black solid curve with grey shaded region shows the best-fitting $\beta = 0$ model with its statistical uncertainties; the orange dot–dashed and blue dotted curves show the best-fitting models with $\beta = -0.5$ and $+0.5$, respectively; the green short dashed curve shows the adopted $\beta(r)$ model of equation (7). The purple dot-long-dashed line shows the best cosmologically based model ['NFW + $\beta(r)$'] and the red double-dot-dashed curve is the logarithmic potential model with $\beta(r)$ (see Sections 4.2.5 and 4.2.6). The horizontal blue long-dashed line with surrounding shaded region shows the stellar *M*/*L* and its uncertainty.

the pseudo-inversion mass approach from R+03, which was based on a different photometric model and a much more limited data set: $\Upsilon_{5,B} = 5.6$–$8.0\,\Upsilon_{\odot,B}$ (distance assumption revised, and only the β uncertainty included).

To further contextualize our result, we calculate the *M*/*L* gradient parameter introduced by N+05:

$$\nabla_\ell \Upsilon \equiv \frac{R_\mathrm{e}\,\Delta\Upsilon}{\Upsilon_\mathrm{in}\,\Delta R}, \tag{8}$$

where Υ_in is the central dynamical *M*/*L*. This parameter is independent of the bandpass and the distance, and is fairly insensitive to the modelling details within the spherical Jeans formalism (with the exception of anisotropy). For simple interpretations we can assume that Υ_in is dominated by the stars as in the case of NGC 4494, but independently of this assumption, the $\nabla_\ell\Upsilon$ parameter has been found to show strong observational correlations with other galaxy properties (N+05). For NGC 4494, we find $\nabla_\ell\Upsilon = 0.02$–$0.23$. This result is nearly identical to our previous finding, placing the galaxy among the population of low-$\nabla_\ell\Upsilon$ (i.e. low-DM) systems (see N+05 and Ferreras, Saha & Williams 2005).

For NGC 3379, the mass-inversion results of D+07 imply $\nabla_\ell\Upsilon = -0.03$–$0.14$. The two galaxies thus appear to have consistent amounts of DM given the total uncertainties, but assuming the *same* anisotropy profile for both, the two galaxies are just barely consistent at the 1σ level. The reason for this difference is that the dispersion profile of NGC 4494 is shallower than that of NGC 3379 (see Section 3.3), while its stellar luminosity falls off more *steeply* (which is a factor that should *steepen* the dispersion profile).

We can also independently estimate the amount of mass contained in the stars (i.e. the stellar M/L, Υ_*) via independent modelling of the stellar population based on line strengths. Unfortunately, there is not a radially extended population map of NGC 4494 available as for NGC 3379, and we are forced to resort to constraints on its very central regions. Based on luminosity-weighted line strengths reported inside ∼1.2 arcsec (Trager et al. 1998), we use the online Worthey (1994) models[9] to estimate an age of ≃10.6 Gyr and a metallicity of [Fe/H] ≃ +0.21, implying $\Upsilon_{*,B} \simeq 4.3 \pm 0.7\,\Upsilon_{\odot,B}$ [Kroupa initial mass function (IMF) assumed, and ∼20 per cent typical age errors adopted from Trager et al. 2000].[10] A caveat here is that the central line indices in general are very likely to be contaminated by young stellar subpopulations confined to the central regions (e.g. in the nuclear disc of NGC 4494) and thus to produce lower Υ_* values than in the halo regions that concern us.

We plot the Υ_* value in Fig. 11, and see that it is similar to the dynamically inferred *M*/*L* in the galaxy's centre. Although there are large uncertainties in this comparison, the coincidence of the best-guess *M*/*L* values suggests that the stars contribute the large majority of the mass in the central regions (similar conclusions were found in the case of NGC 3379 by D+07; see also Gerhard et al. 2001). It is only outside $\sim 2\,R_\mathrm{e}$ where the effects of DM become notable. In the next section we will attempt to constrain Υ_* by dynamical means, and to reconstruct the DM profile in more detail.

4.2 Multi-component models

We now move beyond the pseudo-inversion mass method used in R+03, D+07 and Section 4.1, and construct physically based dynamical models of NGC 4494, allowing for more direct comparisons of observation and theory. Along with these models, we include a kurtosis-based application for alleviating the mass-anisotropy degeneracy. This approach has similarities to the orbit models used for NGC 3379 in R+03, as we will discuss in Section 4.2.3. It is outside the scope of this paper to construct fully rigorous and general dynamical models. Rather, our aim is to generate plausible 'best-guess' models that reproduce the broad features of the data.

Our two-component mass model is simple but realistic, consisting of a luminous field star distribution and (optionally) a DM halo. The total gravitational potential may thus be expressed as $\Phi = \Phi_* + \Phi_\mathrm{d}$. The stellar gravitational potential $\Phi_*(r)$ is derived from the stellar luminosity $j_*(r)$ (according to the Sérsic model of Section 3.1), combined with some assumed constant Υ_*.

We first describe our suite of mass models, where the DM distribution follows either the NFW profile (Section 4.2.1) or a pseudo-isothermal form (Section 4.2.2). Our dynamical methods are outlined in Section 4.2.3, and our results are given in Sections 4.2.4–4.2.6.

4.2.1 NFW model

Our first suite of mass models is based on simulations of collisionless DM halo formation in a ΛCDM cosmology. In this case the DM density takes the approximate form of a NFW profile:

$$\rho_\mathrm{d}(r) = \frac{\rho_\mathrm{s}}{(r/r_\mathrm{s})(1 + r/r_\mathrm{s})^2}, \tag{9}$$

[9] http://astro.wsu.edu/worthey/dial/dial_a_model.html

[10] Somewhat lower Υ_* values are implied by the results of Gerhard et al. (2001), Denicoló et al. (2005) and Zhang et al. (2008), while higher values would be obtained using a Salpeter IMF (Salpeter 1955).

where ρ_s and r_s are the characteristic density and scale radius of the halo. The cumulative dark halo mass is

$$M_d(r) = 4\pi\rho_s r_s^3 A(r/r_s), \tag{10}$$

where

$$A(x) \equiv \ln(1+x) - \frac{x}{1+x}. \tag{11}$$

The potential is

$$\Phi_d(r) = \frac{4\pi G\rho_s r_s^3}{r} \ln \frac{r_s}{r+r_s}, \tag{12}$$

where G is the gravitational constant.

The three free parameters describing the NFW mass model are thus Υ_*, ρ_s and r_s. The halo can alternatively be parametrized by the virial mass and concentration, $M_{vir} \equiv 4\pi\,\Delta_{vir}\rho_{crit} r_{vir}^3/3$ and $c_{vir} \equiv r_{vir}/r_s$, where the critical density is $\rho_{crit} = 1.37 \times 10^{-7}\,M_\odot\,pc^{-3}$ and the virial overdensity value is $\Delta_{vir} = 101$. The expected values for these model parameters are not arbitrary in ΛCDM – a theme to which we will return in Section 5.

4.2.2 LOG model

Our second mass model consists of a logarithmic potential (Binney & Tremaine 1987, Section 2.2.2) which was motivated by observations of spiral galaxy rotation curves (Persic, Salucci & Stel 1996). The potential is

$$\Phi_d(r) = \frac{v_0^2}{2} \ln\left(r_0^2 + r^2\right), \tag{13}$$

where v_0 and r_0 are the asymptotic circular velocity and core radius of the halo. The corresponding DM density and cumulative mass profiles are, respectively,

$$\rho_d(r) = \frac{v_0^2\left(3r_0^2 + r^2\right)}{4\pi G\left(r_0^2 + r^2\right)^2} \tag{14}$$

and

$$M_d(r) = \frac{1}{G}\frac{v_0^2 r^3}{r_0^2 + r^2}. \tag{15}$$

The three free parameters of this 'LOG' model are thus Υ_*, v_0 and r_0. We define a virial mass according to the same definition as in Section 4.2.1.

Unlike the cuspy r^{-1} density core of the NFW halo, the DM density of the LOG halo is constant in the centre. Outside of the core, the density decreases as r^{-2} to produce a constant circular velocity profile $v_c \equiv GM(r)/r^2$, similar to the NFW model near $r = r_s$. Such a model allows us to maximize the stellar contribution to the mass in the central regions, and thus test a 'minimal DM halo' scenario. Similar models have been used to successfully fit galaxies of all types (e.g. Fall & Efstathiou 1980; Begeman, Broeils & Sanders 1991; Burkert 1995; Kronawitter et al. 2000; Thomas et al. 2007; Weijmans et al. 2008; De Lorenzi et al. 2008a, hereafter DL+08a; DL+08b).

4.2.3 Dynamical methods

The Jeans modelling approach employed here is more traditional than that of Section 4.1: one starts with a trial mass model, solves equilibrium equations for the internal velocity moments and projects those moments on to the sky for comparison with the data. This approach typically means solving for the second-order velocity moments (i.e. the velocity dispersions) and comparing to projected velocity dispersion data. However, such data cannot constrain the mass model without additional strong assumptions; the entire LOSVD in a spherical system is necessary to have any hope of uniquely determining its phase-space distribution (e.g. Dejonghe & Merritt 1992). In practice, the systematic uncertainties can be strongly reduced by using fourth-order moments of the LOSVD to diagnose orbit anisotropies (e.g. Gerhard 1993).

One such method is to construct fourth-order Jeans equations in addition to the usual second-order, and to constrain them with kurtosis data (e.g. Magorrian & Ballantyne 2001; Łokas 2002; Łokas & Mamon 2003). Although the higher-order Jeans equations are not closed in general, one can adopt a simple choice for the distribution function which makes the problem tractable (see Appendix B). This simplification is arbitrary (e.g. β is assumed to be constant with radius) and does restrict the generality of our results, but the model is still more general than an assumption of isotropy. Given these restrictions, we can now constrain β using the data.

The basic steps of our analysis are as follows, with details for Steps (ii) and (iii) provided in Appendix B.

(i) Set up a multi-dimensional grid of model parameter space to explore, including β and the mass profile parameters (Υ_*, ρ_s, r_s) or (Υ_*, v_0, r_0).

(ii) For each model grid-point, solve the second- and fourth-order Jeans equations.

(iii) Project the internal velocity moments to σ_{los} and κ_{los}.

(iv) Compute the χ^2 statistics, defined as

$$\chi^2 = \sum_{i=1}^{N_{data}} \left(\frac{p_i^{obs} - p_i^{mod}}{\delta p_i^{obs}}\right)^2, \tag{16}$$

where p_i^{obs} are the observed data points (σ_{los} and κ_{los}), p_i^{mod} the model values and δp_i^{obs} the uncertainties on the observed values, all at the radial position R_i. We fit the PN data outside 40 arcsec and the stellar dispersion between 20 and 60 arcsec. The stellar kurtosis is used between 30 and 60 arcsec.

(v) Find the best-fitting parameters minimizing the χ^2. In practice, we find that the VD is affected by both the mass and anisotropy profiles, while the kurtosis is almost entirely driven by the anisotropy.

For comparison, R+03 modelled NGC 3379 with a similar suite of spherical mass profiles in non-parametric orbit models (A.K.A. 'Schwarschild's method') that included direct fits to the stellar h_4 moments as well as to the full PN LOSVDs. Such methods (see also Chanamé, Kleyna & van der Marel 2008 and DL+08b) may be more powerful than our Jeans approach, but the latter is computationally faster and somewhat more intuitive.

4.2.4 Results: no-DM case

We start with the simplest model, assuming a pure-stellar potential ($\rho_s = 0$ or $v_0 = 0$) and isotropy for the velocity ellipsoid ($\beta = 0$). The best-fitting parameters of the model are given in Table 5 together with their χ^2 values. Given the freedom to adjust Υ_*, this model can fit the VD in the central regions ($\lesssim 2\,R_e$), but falls off too quickly in the outer regions (Fig. 12, upper left). Although the kurtosis is included in the fit (Fig. 12, upper right), omitting these constraints would not provide an appreciably better fit to the VD, since the $M(r)$ and β assumptions already specify fully the shape of the VD. Note that in R+03 we *were* able to fit a pure-stellar model to the VD data, with the difference caused by a slightly steeper new

Table 5. Summary of best-fitting multi-component model parameters.

Model	β_5[1]	Υ_*[2] ($\Upsilon_{\odot,B}$)	$\log M_*$[3] ($M_\odot$)	$c_{\rm vir}$[4]	$\log M_{\rm vir}$[5] ($M_\odot$)	$f_{\rm vir}$[6]	$f_{\rm DM,5}$[7]	$\Upsilon(R_{\rm e})$[8] ($\Upsilon_{\odot,B}$)	Υ_{B5}[9] ($\Upsilon_{\odot,B}$)	$\Upsilon(R_{\rm vir})$[10] ($\Upsilon_{\odot,B}$)	$\nabla_\ell\Upsilon$[11]	χ^2/d.o.f.[12]
					No-DM model							
Star iso	0	4.6	11.04 ± 0.06	–	11.04 ± 0.06	0	0	4.6	4.6	4.6	0	25/37
Star tang	-1.3	4.4	11.02 ± 0.06	–	11.02 ± 0.06	0	0	4.4	4.4	4.4	0	27/36
					NFW model							
NFW iso	0	4.1	$10.99^{+0.05}_{-0.07}$	$6.9^{+0.5}_{-0.4}$	12.03 ± 0.12	10 ± 3	0.41 ± 0.08	$4.5^{+0.2}_{-0.1}$	7^{+1}_{-1}	45^{+10}_{-8}	0.14	21/35
NFW + β_0	0.46 ± 0.15	4.3	$11.01^{+0.05}_{-0.06}$	$6.5^{+1.6}_{-0.6}$	$12.17^{+0.16}_{-0.20}$	13 ± 5	0.42 ± 0.07	$4.7^{+0.3}_{-0.2}$	7^{+2}_{-1}	62^{+21}_{-19}	0.15	10/34
NFW + $\beta(r)$	0.43 ± 0.05	4.1	$10.99^{+0.05}_{-0.07}$	$8.3^{+0.9}_{-0.7}$	12.05 ± 0.10	11 ± 3	0.44 ± 0.08	$4.6^{+0.2}_{-0.2}$	8^{+1}_{-1}	47^{+8}_{-6}	0.14	5/22
					LOG model							
Model	β_5[1]	Υ_*[2] ($\Upsilon_{\odot,B}$)	$\log M_*$[3] ($M_\odot$)	v_0[13] (km s^{-1})	$\log M_{\rm vir}$[5] ($M_\odot$)	r_0[14] (arcsec)	$f_{\rm DM,5}$[7]	$\Upsilon(R_{\rm e})$[8] ($\Upsilon_{\odot,B}$)	Υ_{B5}[9] ($\Upsilon_{\odot,B}$)	$\Upsilon(R_{\rm vir})$[10] ($\Upsilon_{\odot,B}$)	$\nabla_\ell\Upsilon$[11]	χ^2/d.o.f.[12]
LOG iso	0	4.3	$11.01^{+0.07}_{-0.06}$	147	12.19 ± 0.18	244	0.34 ± 0.14	$4.4^{+0.1}_{-0.1}$	7^{+2}_{-1}	65^{+23}_{-20}	0.11	12/35
LOG+β_0	0.44 ± 0.10	4.3	$11.01^{+0.05}_{-0.06}$	172	12.39 ± 0.15	205	0.45 ± 0.13	$4.4^{+0.2}_{-0.1}$	8^{+2}_{-2}	100^{+30}_{-25}	0.18	10/34
LOG+$\beta(r)$	0.43 ± 0.07	4.3	$11.01^{+0.05}_{-0.06}$	146	12.19 ± 0.18	190	0.39 ± 0.16	$4.4^{+0.2}_{-0.1}$	7^{+2}_{-1}	65^{+25}_{-20}	0.15	4/22

Notes. (1) Anisotropy at the benchmark radius of 5 $R_{\rm e}$; (2) dynamical stellar *M*/*L*, in *B*-band solar units: typical uncertainty is $\pm 0.2\Upsilon_{\odot,B}$; (3) log of stellar mass in solar units; (4) concentration parameter (see Section 4.2.1); (5) log of virial mass; (6) ratio of total dark and luminous matter within the virial radius, $f_{\rm vir} = M_{\rm d}/M_*$ at $r_{\rm vir}$; (7) DM fraction, $f_{\rm DM} = M_{\rm d}/(M_{\rm d} + M_*)$ at 5 $R_{\rm e}$; (8) dynamical *M*/*L* at $R_{\rm e}$; (9) dynamical *M*/*L* at 5 $R_{\rm e}$; (10) dynamical *M*/*L* at the virial radius; (11) *M*/*L* logarithmic gradient; (12) χ^2 statistic (see text for details of data included); (13) asymptotic circular velocity: typical uncertainty is ± 30 km s^{-1} and (14) halo core radius: typical uncertainty is ± 50 arcsec.

stellar luminosity profile, by a ∼10 per cent lower VD normalization from the new stellar kinematics data, and by a shallower outer VD slope as derived from our larger, more extended new PN data set.

In order to increase the VD at large radius, we experiment with introducing a degree of tangential anisotropy ($\beta < 0$). As seen in Fig. 12, this strategy does improve the VD fit (best-fitting $\beta = -1.3$), but requires a negative kurtosis in the halo that is ruled out by the PN data. Given the observational uncertainties in the stellar luminosity profile $j_*(r)$ (Section 3.1), we test out a shallower outer profile (Sérsic index $m = 5.2$).[11] We find that we can indeed improve the fit to the VD, but the kurtosis is still problematic for this model. The use of higher-order velocity moments therefore leads us to conclude that there is a non-zero amount of DM in NGC 4494 (as also found by R+03, D+07 and DL+08b for NGC 3379).

Given the presence of DM in this system, we next determine what halo parameters are best consistent with the data for the two assumed DM profiles.

4.2.5 Results: NFW model

Once again, we start by assuming isotropy, and find a best fit as shown in the central panels of Fig. 12, with parameters again reported in Table 5. Note that inside ∼50 arcsec ∼$R_{\rm e}$, both the stars-only and the stars+DM models can recover the VD profile with simple assumptions, suggesting that in these regions it is the stellar mass that determines the main kinematical features.

The isotropic NFW solution is a reasonably good match to the data, but it can be seen that the predicted outer VD is somewhat too high, and the predicted kurtosis somewhat low.[12] Therefore, we next allow for the anisotropy β to be a free parameter, though constant with the radius. The best-fitting solution has a χ^2 value decreased by 9, although there is only one less degree of freedom. This implies that the anisotropic model is strongly preferred over the isotropic one, as also visible in Fig. 12, where both the VD and the kurtosis are at last reproduced well at all fitted radii. The solution has a moderate degree of radial anisotropy ($\beta \sim 0.5$), and is formally preferred at the 3σ level over the best anisotropic stars-only solution; the inferred mass profiles are dramatically different, with the NFW model $v_{\rm c}$ remaining much flatter with radius than the stellar model (see Fig. 13). The radial anisotropy decreases the VD at ∼$R_{\rm e}$ and requires a slightly higher Υ_* value than in the isotropic case.

The halo parameters in this anisotropic analysis are illustrated by Fig. 14, which shows the joint region of permitted values for $r_{\rm s}$ and $\rho_{\rm s}$, marginalized over the other free parameters, Υ_* and β_0. It can be seen that there is a limited degeneracy between the parameters, with alternatively low-$\rho_{\rm s}$ and high-$r_{\rm s}$ models (corresponding to high $M_{\rm vir}$ and low $c_{\rm vir}$), or high-$\rho_{\rm s}$ and low-$r_{\rm s}$ (low $M_{\rm vir}$ and high $c_{\rm vir}$).

The best-fitting anisotropy value in our modelling of $\beta = 0.46$ is remarkably similar to theoretical expectations for galaxy haloes (see Section 4.1). Therefore, in order to make an improved estimate of a plausible ΛCDM halo that would reproduce our data, we adopt equation (7) for the anisotropy profile $\beta(r)$. This model is isotropic in the centre and radially anisotropic in the outer parts, where the transition radius $r_{\rm a}$ is free to vary (within the range 30 to 110 arcsec). Because our Jeans modelling procedures are not entirely designed to cope with a radially varying β (see Appendix B), we adopt a slightly different procedure than the preceding. We fit the VD data as before, but fit the kurtosis data only at large radii ($R > 100$ arcsec), where the anisotropy is fairly constant, and considered fixed to its value at 200 arcsec (∼4$R_{\rm e}$); see equation (B8).

This final best-fitting theoretically motivated model is again a good match to the data (see Fig. 12 and χ^2 in Table 5). The anisotropy transition radius is $r_{\rm a} = 45 \pm 20$ arcsec, i.e. radial anisotropy may set in at smaller radii in NGC 4494 than in the

[11] Our surface photometry is originally *g* band transformed to the *B* and *V* bands, so the true stellar mass density profile (∼*K* band) is likely to be *steeper*.

[12] Although a galaxy halo with $\beta = 0$ and constant $v_{\rm c}$ should result in $\kappa_{\rm los} = 0$, our mass model deviates enough from this picture to produce non-zero kurtosis.

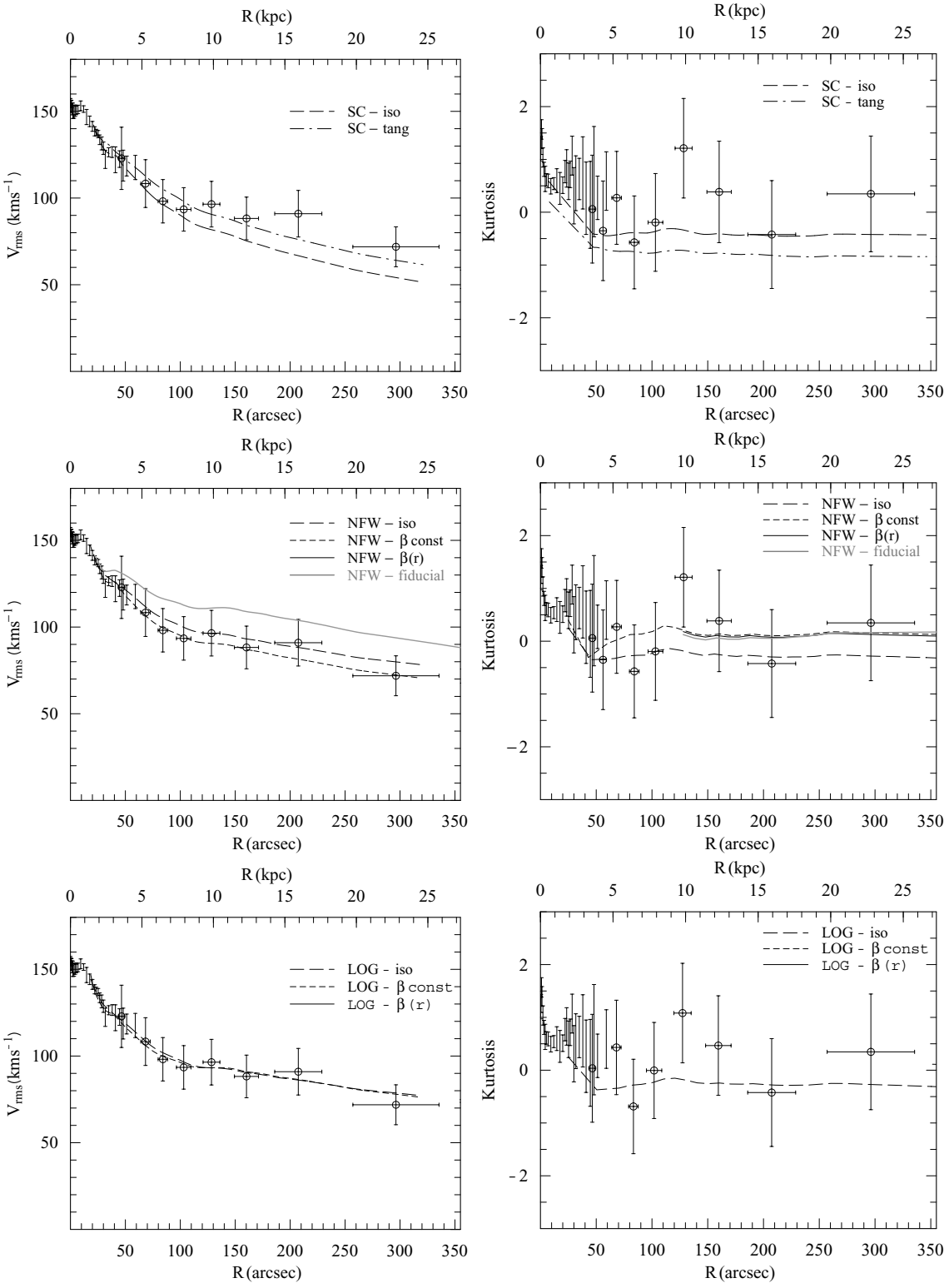

Figure 12. Multi-component Jeans model fits to the NGC 4494 kinematics data. The stellar data are shown by star symbols, while the PN data are open circles. The left-hand panels show the projected rms velocity profiles, while the right-hand panels show the projected kurtosis. The top panels show fits from self-consistent stars-only models, the central panels show stars+NFW halo models and the bottom panels show stars+LOG halo models. The curves correspond to models as in the panel legends (see text for details).

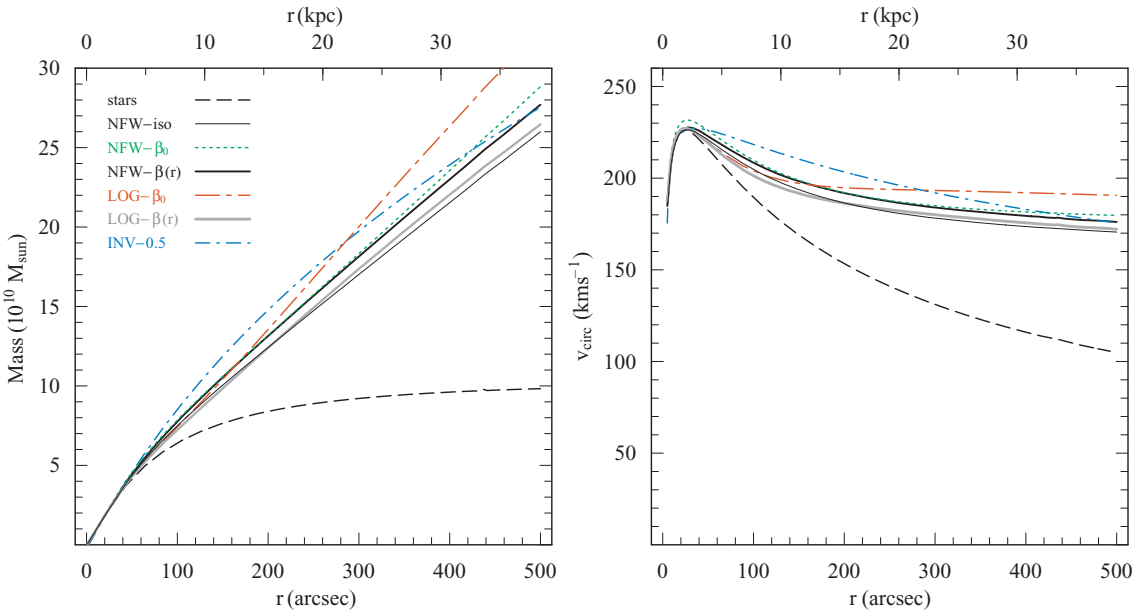

Figure 13. Radial mass distribution of NGC 4494. The left-hand panel shows the cumulative mass and the right-hand panel shows the circular velocity profile. The heavy solid curves are the best-fitting stars+DM model with varying anisotropy (black is NFW, grey LOG) while the light black solid line is the isotropic NFW case; the dashed curve is the stellar distribution for the LOG model ($\Upsilon_* = 4.3\Upsilon_{\odot,B}$). The green dotted curves show the $\beta = 0.5$ stars+NFW model and the red dot-long-dashed curves the $\beta = 0.5$ stars+LOG model while the blue dot–dashed curves show the $\beta = 0.5$ pseudo-inversion mass result. A legend for the model symbols is in the left-hand panel.

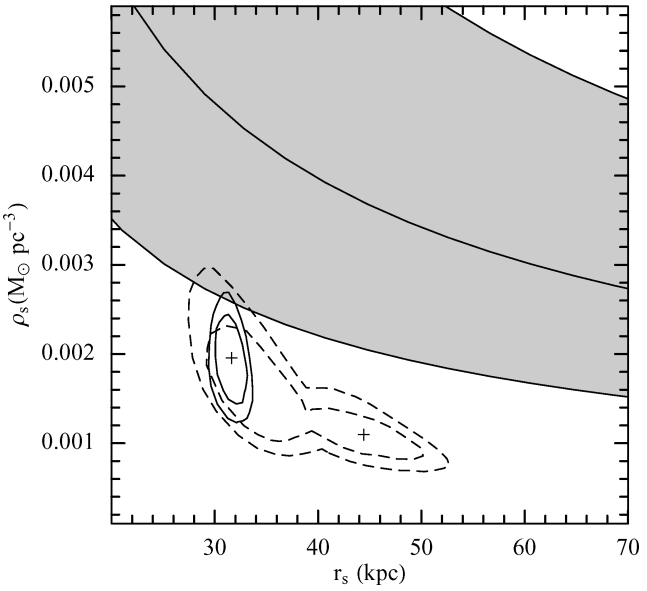

Figure 14. Halo parameter solutions for NGC 4494 NFW-based model, plotted as halo scale radius r_s versus central density ρ_s. The contours show the two-parameter χ^2 confidence levels (1σ and 2σ). Dashed contours show the constant-β model, and solid contours the $\beta(r)$ model. The best-fitting solutions are marked with crosses. The solid line with shaded region shows the theoretical expectations for the halo parameters (see Section 5.2) and the 1σ scatter.

simulations of D+05. The stellar M/L of this solution of $\Upsilon_{*,B} = 4.1 \pm 0.2\Upsilon_{\odot,B}$ agrees remarkably well with the independent estimate from stellar populations of $\Upsilon_{*,B} \simeq 4.3\,\Upsilon_{\odot,B}$ (Section 4.1). The central NFW halo parameters of $\rho_s = 0.0019 \pm 0.0006\,M_\odot\,pc^{-3}$ and $r_s = 410 \pm 30$ arcsec $= 32 \pm 2$ kpc correspond to a virial radius, mass and concentration of $r_{vir} = 261 \pm 30$ kpc, $M_{vir} = (1.12^{+0.33}_{-0.24}) \times 10^{12}\,M_\odot$ and $c_{vir} \sim 8 \pm 1$.

As shown in Fig. 14, this $\beta(r)$ solution is better constrained than the constant-β one, and coincides with its secondary χ^2 minimum –showing that the results were not sensitive to the potentially worrisome stellar kurtosis points between 30 and 60 arcsec. The data in both models are inconsistent at the $\sim 1\sigma$ level with the predicted relation from ΛCDM [shown in the same figure, see equation (19) in Section 5.2]. As a visual demonstration of the significance of this result, in Fig. 12 we show also a 'typical' expected ΛCDM halo, with $c_{vir} = 12.3$ and $M_{vir} = 2 \times 10^{12}\,M_\odot$, and a $\beta(r)$ profile with $r_a = 67$ arcsec. This model is a relatively poor fit to the dispersion profile, and requires a smaller $\Upsilon_*(=3.4\Upsilon_{\odot,B})$ in order to match the central data points. On the other hand, the kurtosis is well matched, as the anisotropy profile is similar to our best-fitting NFW + $\beta(r)$ model.

4.2.6 Results: LOG model

We next carry out an equivalent model sequence for the LOG halo model, with results shown in Fig. 12 (bottom) and Table 5. For the cases of $\beta = 0$ or $\beta =$ const, the LOG model can fit the data significantly better than the NFW model, owing to the former's slower transition with radius from stellar to DM dominance. In the case of variable anisotropy, the LOG and NFW models have comparably good fits and similar $\beta(r)$ profiles, but in the context of the LOG model, we cannot distinguish between the different β models. However, we will adopt the $\beta(r)$ solution as the best LOG model because of its theoretical motivation.

The M/L at $5R_e$ is very similar for the $\beta(r)$ NFW and LOG models, demonstrating that this quantity is well constrained by the data, independently of the details of the mass models. The mass profiles are also similar given the modelling uncertainties (Fig. 13),

with the NFW model assuming a relatively low concentration which mimics the constant-density core of the LOG model, and with the NFW scale radius value of $r_s \sim 9\ R_e$ producing a roughly flat v_c profile in the halo regions as in a LOG model. The remaining differences in the model profile shapes result in slightly different values for Υ_*, which is lower for the NFW model because of the stronger central DM contribution from its cuspy core.

Although we cannot at this stage distinguish between the NFW and LOG models, there are possibilities for doing so in the future. New data extending to larger radii could verify our current results and provide stronger discriminants between the mass models surveyed here and alternative ones – but would not be able to discriminate between the NFW and LOG models, which begin to diverge only near the virial radius (note the differing extrapolated M_{vir} values in Table 5). More crucial would be generalized modelling which fits the fine details of the stellar kinematics in order to tease out the differences in the total mass profile shapes in the central regions. In this context, additional data over a wide baseline in radius would also help to build up the S/N of the constraints.

4.3 Systematics and mass comparisons

We next investigate the sensitivity of our mass results to some systematic issues and to different modelling methods and mass tracers. We can first examine the results from the different modelling methods and assumptions we have used thus far. As seen in Figs 11 and 13, the total mass profile at the outer extent of the data ($\sim$300 arcsec) is fairly well determined (within $\sim \pm 30$ per cent) regardless of the anisotropy and mass model assumptions, and of the Jeans method used (cf. also the consistency of the Υ_{B5} benchmark parameter in Table 5). Similarly, the inferred value for Υ_* is the same at the $\sim \pm 5$ per cent level, and is reassuringly consistent with the independent estimate from stellar populations analysis. Using the more detailed models of Section 4.2 with their anisotropy constraints, we update our estimate of the M/L gradient (Section 4.1) to $\nabla_\ell \Upsilon \sim$ 0.1–0.2.

One caveat about all of these Jeans models is that a somewhat arbitrary radial region is chosen for fitting the central stellar kinematics (thereby normalizing the entire solution), since the models are not sufficiently flexible to reproduce the high S/N bumps and wiggles representing fine structure in the stellar data. The only such model to date of NGC 4494 was by Kronawitter et al. (2000), based on spherical non-parametric distribution function fitting. Using the B+94 stellar kinematics data set, they found a circular velocity profile at $\sim 0.5\ R_e$ which is slightly different from ours (perhaps owing to the data differences; see Section 3.4). Similar results without the benefit of h_4 constraints were found by Magorrian & Ballantyne (2001).

It is of critical importance for more fully understanding this system to employ a more general dynamical model that can fit the stellar data in detail, while not requiring the Łokas-type simplification (see Appendix B) we have imposed on the distribution function. There are already some indications from our Jeans modelling that other regions of model space may be permitted (with lower Υ_* and higher central DM content). While more general modelling is outside the scope of this paper, we can estimate the possible systematic effects from the Jeans smoothing simplifications. In the generalized NMAGIC modelling of NGC 3379 (DL+08b), the halo anisotropy could not be constrained to better than $\Delta\beta \sim \pm 0.3$. Taking this as a guide, we re-run our NFW-based Jeans models with β_0 fixed at either $+0.2$ or $+0.8$, finding that the corresponding systematic uncertainty in c_{vir} is then ± 1.8, and in $\log M_{vir}$ is ± 0.26.

Our models make powerful use of the assumption that the PNe and field stars are drawn from the same underlying dynamical population. This premise was questioned by D+05, who posited that the PNe could reflect a recent burst of star formation with distinct dynamics from the observed field stars – a hypothesis with some support from observations (Sambhus, Gerhard & Méndez 2006; Forestell & Gebhardt 2008). We discussed this issue in more detail in D+07 and Coccato et al. (2008), and here note that NGC 4494, although a reasonable candidate for a young stellar subpopulation (Denicoló et al. 2005), in fact shows good agreement between its PN and stellar properties (see e.g. Section 3.1).

Our ΛCDM mass models assume a fairly basic collisionless NFW form for the DM distribution. This profile is bound to be altered by interaction with the collisional baryons; although the amount and even the sign of the effect are not clear, the standard view is that the change can be approximated by adiabatic contraction (e.g. Gnedin et al. 2004). The effect of this contraction would be to draw more DM into the central regions, flattening the rotation curve, and thereby requiring a lower stellar M/L (possibly losing the consistency of our solution with the independent value) and a lower concentration. A more recent revision of the collisionless DM distribution (the Einasto model; Gao et al. 2008) would tend to push things in the opposite direction, but more weakly. Of course, these conventional mass-model pictures could be completely wrong, as we have seen that a cored-halo model fits our data equally well (see also e.g. de Blok, McGaugh & Rubin 2001; Borriello, Salucci & Danese 2003; Gentile et al. 2007), and alternative gravity models should also be explored (e.g. Tiret et al. 2007).

A final concern, and a perennial problem in modelling any galactic system, is the symmetry assumption. The spherical symmetry adopted here has in particular been called repeatedly into question, and certainly more robust results should eventually be derived using less restrictive symmetries and more detailed modelling. NGC 3379 is a similar case to NGC 4494, where its round apparent shape could be produced by a very flattened system seen near face-on. DL+08b used flattened particle-based 'NMAGIC' models of NGC 3379 to explore the simultaneous effects of shape and anisotropy on the mass inferences from PNe. Intriguingly, they found that relaxing the spherical assumption hardly affects the inferred halo mass: the intrinsic flattening and inclination are strongly limited by the observed rotation field, and the main source of systematic uncertainty remains the halo anisotropy (which the available data do not constrain). Thus, the effects of asphericity on mass modelling may not be as important as previously thought (cf. Bekki & Peng 2006), although the effects of triaxiality have yet to be fully explored.

It is beyond the scope of the current paper to construct similar advanced models for NGC 4494, but we do explore a flattened scenario using similar Jeans machinery to Section 4.2, as described in Appendix C. We find that the inferred DM halo differs little from our spherical conclusion. It will be the object of a future paper to fully explore multiple modelling methods with NGC 3379, NGC 4494 and other galaxies to get a handle on the robustness of the results to the methods. But so far, although very general models allow a wider range of solutions, we have seen no evidence that these models imply a systematic shift in the preferred mass solutions.

Fully independent mass constraints from another observational tracer such as GCs or X-ray emitting gas are desirable. O'Sullivan & Ponman (2004) analysed *XMM–Newton* observations of NGC 4494, finding a weak component of very soft ($k_B T_X \sim 0.2$ keV) X-ray emitting gas in a compact arrangement (within $\sim R_e$). They proposed that the X-ray underluminosity of this and similar ETGs could be due to either a weak or diffuse DM halo, or to a young field star

population which has had little time to build up an X-ray halo through winds (though there are problems with this scenario). More recently, it was suggested that the apparent emission from hot gas in such galaxies may in fact be dominated by cataclysmic variables and coronally active binaries (Sazonov et al. 2006; Revnivtsev et al. 2008).

Whether or not it is feasible to measure the halo mass of NGC 4494 using hot gas is thus a very open question. Assuming that there is any such gas which could be studied with deeper observations, it is more likely to be in an outflowing wind state than in hydrostatic equilibrium, which would greatly complicate the mass analysis (Pellegrini & Ciotti 2006). Given these caveats, we note that Fukazawa et al. (2006) did derive a basic mass estimate for NGC 4494 from *Chandra* observations of apparent compact X-ray gas emission. They found an M/L of $6.2 \pm 1.9\ \Upsilon_{B,\odot}$ inside 1 R_e (converted to our distance, with minimal uncertainties estimated from the uncertainty in T_X), which is consistent with our finding of $\sim 4.5 \Upsilon_{B,\odot}$ at this radius (see Fig. 11). Note though that a different analysis by Diehl & Statler (2007) found no trace of X-ray gas in this system.

5 IMPLICATIONS: ORDINARY ELLIPTICALS REVISITED

Given the dynamical solutions found for NGC 4494 in Section 4.2, we compare them to other galaxies, and consider the possible implications for DM and for galaxy formation. We start with a small sample of galaxies consisting of all four 'ordinary' ellipticals discussed in R+03, whose PN dynamics originally suggested unexpectedly low DM content: NGC 821, NGC 3379, NGC 4494 and NGC 4697 [with data from the latter presented in Méndez et al. (2001)]. These galaxies have similar central velocity dispersions $\sigma_0 \sim 200$ km s^{-1} and near-L^* luminosities ($M_B \sim -20.3$; see Table 6), and are of the discy/cuspy ETG sub-type found by N+05 to have lower DM content on $\sim 5\ R_e$ scales than the boxy/cored ETGs. These galaxies (dubbed the 'R+03 sample') are also of the 'fast rotator' variety of ETG (Section 3.2 and Emsellem et al. 2007), which as a class shows hints of less central DM content than the slow rotators (Cappellari et al. 2006).

Each galaxy has now been modelled using constraints on higher-order LOSVD moments to handle the mass-anisotropy degeneracy, and to infer the Υ_* component by dynamical means: NGC 821 using three-integral axisymmetric orbit models (stellar kinematics only; Forestell & Gebhardt 2008, but see also preliminary analysis of PN kinematics in Napolitano et al. 2007); NGC 3379 using spherical orbit models (R+03) and spherical, axisymmetric and quasi-triaxial particle modelling (DL+08b); NGC 4494 using kurtosis-based Jeans models and NGC 4697 using axisymmetric particle modelling (DL+08a). One caveat is that these results are tied to particular assumptions about the form of the DM density profile (NFW or LOG), which affects the decomposition of the total mass into stars and DM. For example, dynamics on its own does not completely rule out a scenario (though unrealistic) where the stars have zero mass and the central DM profile is similar to the stellar luminosity profile.

We examine the DM fraction for these galaxies, as well as for theoretical models, in Section 5.1. In Section 5.2, we consider the global DM halo parameters, and in Section 5.3 we place them in the wider context of galaxy formation.

Table 6. Mass results for fast-rotator ETGs, based on extended kinematics data and higher-order LOSVD modelling. The absolute magnitudes M_B and central velocity dispersions M_B and σ_0 are adapted from HyperLeda, D+07 and this work.

Name	M_B	σ_0(km s^{-1})	$\log M_*$ ($M_\odot$)	$\log M_{\rm vir}$ ($M_\odot$)	$c_{\rm vir}$	$\Upsilon_{\rm vir}$ ($\Upsilon_{\odot,B}$)
NGC 821	−20.5	210	11.24	14.46	2.5	1700
NGC 3379	−19.9	207	11.01	12.17	6.1	100
NGC 4494	−20.5	150	10.99	12.05	8.3	47
NGC 4697	−20.2	174	11.14	12.75	6.1	300

5.1 The dark matter fraction

The first basic parameter we consider is the DM fraction within a given radius r:

$$f_{\rm DM}(r) \equiv \frac{M_{\rm DM}(r)}{M_{\rm tot}(r)}, \tag{17}$$

where we find for NGC 4494 from the best-fitting NFW and LOG models that at $5R_e$, $f_{\rm DM,5} = 1 - \Upsilon_*/\Upsilon_5 \sim 0.2$–$0.5$. For NGC 3379, the comparable calculation from the R+03 spherical model yields $f_{\rm DM,5} \sim 0.2$– 0.4 (cf. D+07). The flattened models for NGC 3379 from DL+08b imply $f_{\rm DM,5} \sim 0.2$–0.6, while similar models for NGC 4697 give $f_{\rm DM,5} \sim 0.3$–0.6. These galaxies are therefore all consistent with a typical value of $f_{\rm DM} \sim 0.4$ at 5 R_e; this value is notably lower than one would expect from strong gravitational lensing studies which typically find $f_{\rm DM} \sim 0.3$ at R_e (e.g. Gavazzi et al. 2007), i.e. at much smaller distances from the centre. However, lensing studies so far include very few of the fainter ordinary galaxies which would be equivalent to this fast rotator sample, although there are emerging indications of lower $f_{\rm DM}$ systems (Ferreras et al. 2005; Covone et al 2008). The constraints on NGC 821 (based on stellar kinematics only) do not extend to large enough radii for a direct comparison, and the models do suggest that this galaxy is different, with $f_{\rm DM} \sim 0.5$ at 1.5–2 R_e already. However, our preliminary analysis based on PN kinematics (Napolitano et al. 2007) seems to favour a lower $f_{\rm DM} \sim 0.4$ at 5 R_e, as found for the other three observed galaxies.

On the theoretical side, N+05 found for a simplified ΛCDM-based suite of models that one should expect $f_{\rm DM,5} = 0.5$–0.8, depending on various assumptions about the galaxy and DM masses. A similar framework from MŁ05 predicted $f_{\rm DM,5} \sim 0.5$. Simulations of ETG formation including baryonic processes are now beginning to produce plausible results, with the schematic pair-merger simulations of D+05 yielding $f_{\rm DM,5} \sim 0.5$–0.7. The full cosmological simulations of Naab et al. (2007) and Oñorbe et al. (2007) suggest $f_{\rm DM,5} \sim 0.4$ and ~ 0.6–0.7, respectively (though it is not clear if these simulated galaxies are better analogues of the fast or slow rotators). This variety of predictions are all roughly consistent with a typical $f_{\rm DM,5} \sim 0.5$ (a quantity that is presumably not very sensitive to baryonic effects) – which appears similar to the empirically obtained values.

For additional insight, as in D+07, we show the DM fraction as a function of effective radius in Fig. 15, with various of the aforementioned empirical and theoretical results displayed. The plot is somewhat tricky to interpret because the stellar and DM mass profiles probably do not scale with luminosity in a homologous way. For example, NGC 3379 and the Naab et al. (2007) simulated ETGs have similarly small values for R_e and hence should be compared; the larger galaxies, NGC 4494 and NGC 4697, should presumably be compared to the D+05 and Naab et al. (2007) simulations. It thus becomes clear that simulations which include baryonic effects predict systematically more DM within 5 R_e than is inferred

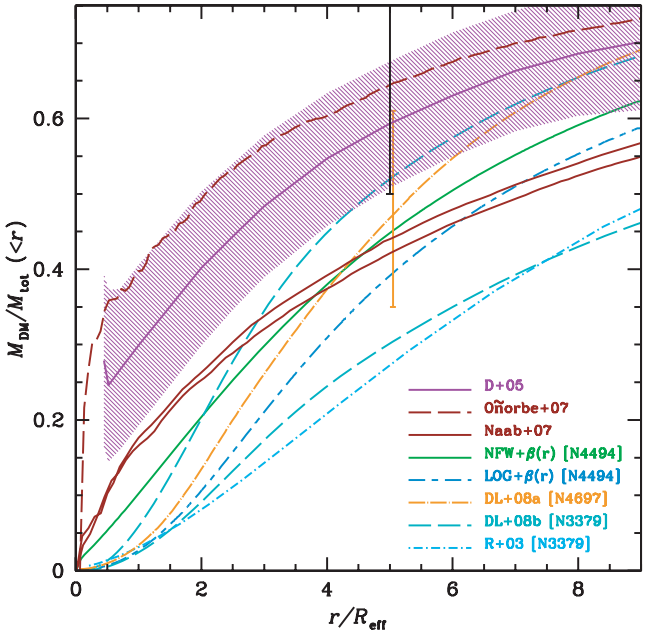

Figure 15. Cumulative DM fraction as a function of radius. The green solid line shows the best-fitting $\beta(r)$ stars+NFW model while the short-long-dashed blue line is the $\beta(r)$ stars+LOG model for NGC 4494: typical uncertainties are 20–30 per cent at 5 R_e (see Table 5) and drop to ∼10 per cent at 1R_e. Light green long-dashed and cyan dot-short-dashed lines are the best-fitting results of NGC 3379: DL+08b (model C90 – lower line, and D90 – higher line) and R+03, respectively. Orange dot-long-dashed line is the DM fraction of NGC 4697 (DL+08a model G with error bar showing the DM fraction at 5 R_e for models D to J). The purple line with surrounding shaded region shows the mean results and scatter from the galaxy merger simulations of D+05. The red lines show simulations from Naab et al. (2007, solid curves) and Oñorbe et al. (2007, dashed curve). The black error bar shows the theoretical prediction from N+05 based on ΛCDM cosmology and the full range of allowed star formation efficiency ($_{SF} = 0.07$–1; see Section 5.2).

observationally, and that this mismatch becomes even stronger at smaller radii.[13]

While the DM fraction $f_{DM,5}$ is a directly constrained observational quantity, its meaning may be muddled by the whims of the baryonic processes in individual galaxies. For example, NGC 4494 appears to be more DM dominated in its central regions than NGC 3379 (Fig. 15), but the global halo properties of the two galaxies turn out to be very similar – even though the PN velocity dispersion in NGC 3379 declines much more steeply than in NGC 4494 (Section 3.3). This suggests that halo VD gradients are strongly affected by the individual galaxy scalelengths, and careful dynamical modelling is necessary to interpret the implications for DM.

5.2 Halo parameters: the R+03 sample

For less ambiguous comparisons to theory, one can instead consider directly the properties of the DM haloes. A halo's virial properties are not directly constrained by PN kinematics data which extend to only ∼ 0.1 r_{vir}, but we can at least hazard some guesses by assuming a priori a functional form for the mass profile to be extrapolated outwards (e.g. the NFW model). Dynamical modelling results based on NFW haloes were presented for NGC 821, NGC 3379 and NGC 4494 in Forestell & Gebhardt (2008), R+03 and this paper, respectively. For NGC 4697, DL+08a used a LOG potential (model H), to which we have fitted a NFW model post hoc. The results are summarized in Table 6, where it should be noted that a cluster mass halo is not credible for the isolated galaxy NGC 821, and is a product of extrapolating from data extending to only 2 R_e. However, the joint mass–concentration result for this galaxy is relevant, as discussed below.

Disregarding NGC 821, we see that the other three galaxies have virial M/L values of ∼50–150 $\Upsilon_{\odot,B}$, and virial DM fractions of ∼91–95 per cent. Assuming a primordial baryon fraction of 0.17 (Hinshaw et al. 2008), this implies that the net star formation efficiency was ∼30–50 per cent for these galaxies. These results are broadly consistent with the current consensus that star formation was most efficient in galaxies near the L^* luminosity (e.g. Marinoni & Hudson 2002; Mandelbaum et al. 2006; van den Bosch et al. 2007).

Rather than measuring the virial mass, the kinematics data are best suited to measure the amount of DM within ∼5 R_e, and to some extent the detailed profile of DM with radius in the same region. In the context of a NFW model, we can determine jointly the mass and concentration parameters M_{vir} and c_{vir}. Given perfect observational constraints from small to large radius, we could uniquely determine these parameters as well as Υ_* based on the detailed shape of the $v_c(r)$ profile. With real-world uncertainties in the observations and the dynamical modelling, there is in practice a strong degeneracy between these parameters, within certain limits (cf. Fig. 14 and MŁ05 fig. 1). Roughly speaking, a larger value of M_{vir} will require a smaller value of c_{vir} (in order to decrease the fraction of DM inside 5 R_e) and a higher value of Υ_* (compensating for the reduced amount of DM in the very central regions).

We show the mass–concentration results (Table 6) for the R+03 sample in Fig. 16 (filled triangles). Except for the case of NGC 4494, the uncertainties are generally not shown because at this juncture they are not uniformly and robustly determined. As previously discussed, the uncertainty regions can be expected to follow a diagonal degeneracy track from low mass and high concentration, to high mass and low concentration. This suggests that the NGC 821 result at $M_{vir} \sim 10^{14}\,M_\odot$ and $c_{vir} \sim 3$ could be consistent with the other three galaxies at $M_{vir} \sim 10^{12}\,M_\odot$ and $c_{vir} \sim 6$.

Next, we can compare these empirical results to theoretical expectations. In a collisionless ΛCDM universe, a mean relation is expected between mass and concentration such as the following:

$$c_{vir}(M_{vir}) \simeq 18 \left(\frac{M_{vir}}{10^{11}\,M_\odot}\right)^{-0.125}, \qquad (18)$$

where the relation has a 1σ scatter of 0.14 dex, and is valid for $z = 0$, $\Omega_m = 0.3$, $\Omega_\Lambda = 0.7$, $h = 0.7$, $\Delta_{vir} = 101$ and $\sigma_8 = 0.9$ (Bullock et al. 2001; N+05). Although more recent work has revised this relation with higher-resolution simulations and updated cosmologies (e.g. Neto et al. 2007; Duffy et al. 2008), the differences below $M_{vir} \sim 10^{14}\,M_\odot$ are only at the level of ∼ 10 per cent. The prediction is thus that higher-mass haloes have lower concentrations, which conveniently coincides roughly with the direction of the uncertainties in the observational results, and means that we can make useful comparisons to theory despite the modelling degeneracies.

As shown in Fig. 16, the R+03 sample suggests a mass–concentration relation that is parallel to the theoretical expectation,

[13] Note that the uncertainty bounds on the observational results are not shown in the figure for the sake of clarity. On a case-by-case basis, few of the galaxies may be formally inconsistent with the theoretical predictions, but the overall mean pattern is a systematic offset between observations and theory – while there is no indication of a systematic shift in the observational results (see also Section 5.2).

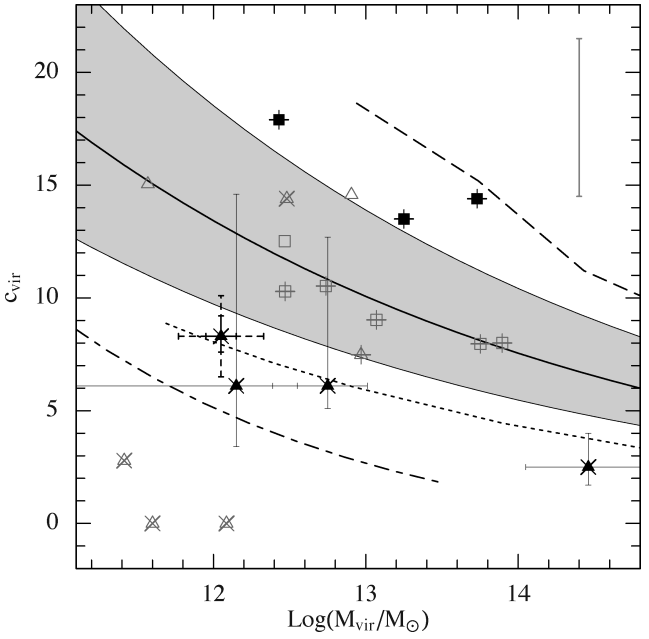

Figure 16. DM halo virial mass and concentration parameters. Triangles and boxes mark fast-rotator and slow-rotator ETGs, respectively. '×' and '+' symbols mark discy/cusped and boxy/cored galaxies, respectively, classified following Faber et al. (1997) and N+05. The filled symbols mark detailed ETG dynamical results using PNe and GCs (light error bars, where available), with solid and dashed heavy error bars showing the statistical and systematic (Section 4.3) uncertainties for NGC 4494. The open symbols show the dynamics-based ETG results from N+05, with error bars in the upper right corner showing the typical uncertainties. The dashed line shows the mean result for X-ray bright groups and clusters, the dot–dashed line is an inference for late-type galaxies and the dotted line is the trend from weak lensing of all types of galaxies and groups. The solid curve with shaded region shows a mean relation expected from ΛCDM, with its 1σ scatter.

but offset to lower concentration values by a factor of ∼2. This discrepancy was also manifested in Section 5.1 as a difference in DM fractions. One could perhaps systematically increase the observed concentrations into agreement with theory, by postulating that all of the galaxies systematically have very radial halo anisotropy (e.g. $\beta \gtrsim 0.8$ at $\sim 7\ R_e$; DL+08b) which may be technically allowed by the data. However, this anisotropy is not consistent with the ΛCDM-based simulations of D+05, nor perhaps with any reasonable theory of galaxy formation: for this ETG sample, it appears difficult to simultaneously fit both the mass and anisotropy profiles of ΛCDM galaxies. However, since the anisotropy is not yet well constrained by observations or by theory, we will continue to focus here on the better-understood issue of mass profiles.

For comparing with models parametrized by the scale radius r_s and density ρ_s (e.g. Fig. 14), we find that equation (18) is equivalent to the following relation:

$$\rho_s \simeq \left(\frac{r_s}{10\,\mathrm{pc}}\right)^{-2/3} \mathrm{M}_\odot\,\mathrm{pc}^{-3}, \qquad (19)$$

where the scatter in ρ_s at fixed r_s is a factor of 1.8.

5.3 Halo parameters: wider context

The mass–concentration comparison will obviously need much more scrutiny using a large observational sample along with rigorous dynamical modelling – which is the goal of our ongoing PN.S survey of ETGs. But, based on the preliminary trend that we see, we may start putting the results in context, starting with some comparisons to previous results for ETGs. For the sake of uniformity, we initially include only studies of ETGs using extended kinematics data fitted to basic NFW-based models as in this paper. These galaxies are NGC 1399, M87 and NGC 4636 – in all cases modelled with a combination of stellar and GC dynamics, though not in all cases directly constraining the anisotropy (Romanowsky & Kochanek 2001; Schuberth et al. 2006; Richtler et al. 2008). Intriguingly, these galaxies' haloes (filled boxes in Fig. 16) all have much higher concentrations than the R+03 sample (by a factor of ∼3–4), and are slightly higher than the theoretical expectation, though consistent within typical modelling uncertainties.

We do not believe this difference is a systematic modelling effect from using PN versus GC dynamics, as our preliminary PN.S work also suggests a population of high-concentration galaxies (Napolitano et al. 2007). The ETG stellar dynamics analysis of Gerhard et al. (2001) found a main sequence of high DM halo densities consistent with the three high-concentration galaxies, along with a few lower-density galaxies similar to the four low-concentration galaxies. A related analysis from Thomas et al. (2007) also found a large scatter in DM halo densities for cluster ETGs.

In order to increase the sample size, we next plot the results from N+05, who used dynamical results on ETGs from the literature to infer NFW-based mass–concentration parameters. We classify the galaxies as fast- or slow rotators based on C+07 where possible, and otherwise using literature results as described in Section 3.2. While these mass inferences are not as individually reliable as direct NFW-based modelling, we do not detect any systematic difference between the two techniques when comparing overlapping cases. Interestingly, the main effect of this supplemental sample is to fill in the 'missing' population of normal-concentration haloes (Fig. 16). Examples of such galaxies include NGC 4406, NGC 5128, NGC 5846 and NGC 6703.

When compared to the theoretical prediction, the overall ETG dynamics-based results suggest a normal population of haloes, with a systematic bias for fast rotators to reside in low-concentration haloes, and slow rotators in high concentrations. Although it is outside the scope of this paper to determine if this difference is more strongly linked to rotation, luminosity, isophote shape, environment, etc., Fig. 16 suggests that isophote shape is at least as important as rotation. The concentration gap seen in the initial sample may be due to selection effects, e.g. the systems with the most GCs amenable to dynamical study would be systematically the most massive systems (Spitler et al. 2008). But, we also note that given no theoretical prejudice, the data themselves would suggest a shotgun pattern of masses and concentrations, with no hint of a systematic decrease of concentration with mass (if anything, the data suggest an *increase*).

Since the initial three high-concentration systems are galaxies at the centres of massive X-ray-bright groups and clusters, we compare the results from a large sample of low-redshift groups and clusters (Duffy et al. 2008), where we have transformed the halo parameters from $\Delta_{vir} = 200$ to 101, and from $z = 0.1$ to 0 by the trend $c_{vir} \sim (1 + z)^{-1}$. As shown in Fig. 16, this relation is similar to (∼15 per cent higher than) the high-concentration dynamical sample. Other studies using gravitational lensing have also found relatively high concentrations for clusters (Comerford & Natarajan 2007; Hennawi et al. 2007; Broadhurst & Barkana 2008; Broadhurst et al. 2008).

We next broaden the picture to include *late-type* galaxies. There is an emerging consensus that such galaxies near the L^* luminosity (including the Milky Way) have NFW-based concentrations that are unexpectedly low (Kassin et al. 2006; Dutton et al. 2007; Gnedin

et al. 2007; McGaugh et al. 2007; Xue et al. 2008; see Macciò, Dutton & van den Bosch 2008 for a differing view). We take the mass–velocity relation from fig. 10 of McGaugh et al. (2007), and adapt it for Fig. 16, where we see that it is similar to the low-concentration ETGs (∼25 per cent lower).

The overall impression we gain from these combined detailed studies of individual systems is of an 'S'-shaped relation, where the galaxy-scale haloes follow a trend of relatively low concentrations, and there is a transition at $M_{\rm vir} \sim 5 \times 10^{12}\,{\rm M}_{\odot}$ to group haloes with higher concentrations. This transition is comparable to the DM 'dichotomy' between low- and high-stellar-mass galaxies found by N+05, occurring at $M_{*} \sim 2 \times 10^{11}\,{\rm M}_{\odot}$.

As a final piece to the puzzle, we consider a recent weak-gravitational-lensing study of both late and ETGs, from galaxy to cluster masses (Mandelbaum, Seljak & Hirata 2008). The mean trend is shown in Fig. 16 (after conversions for $\Delta_{\rm vir}$ and z) and is seen to roughly coincide with the apparent trends for late-types and fast-rotator ETGs, with no indication of the high-concentration trend found by dynamics and by X-rays.

Although there are potential sources of systematic error with any of these mass-measurement techniques, and some of the sample sizes are small, the observational evidence so far agrees on a main population of relatively low-concentration galaxy-scale DM haloes. At higher masses, the observational inconsistency might be resolved if there were a strong selection effect in the X-ray and dynamical studies for high-concentration systems. Alternatively, keeping in mind that weak lensing probes the outer regions of haloes while the other techniques probe the central regions, the inner haloes of groups and clusters might deviate strongly from the assumed NFW profiles.

We next consider some theoretical scenarios that might explain these observational constraints. The impact of baryons on their host DM haloes could be a significant factor; e.g. the observed concentration transition occurs at roughly the same mass scale where a change in the physics of gas cooling and heating is expected (Cattaneo et al. 2006). As discussed in Section 4.3, the standard model for baryonic modification of a collisionless DM halo involves adiabatic contraction, which draws additional DM into the central regions. The implication for inferring unmodified NFW concentrations would be to *decrease* them, i.e. the observational data points in Fig. 16 would be shifted slightly down and to the left. This effect *might* bring the slow-rotator group-central ETGs into agreement with theory, but would make matters worse for the fast-rotator ETGs and the late-types. For those, a strong net halo *expansion* would be required, perhaps as a consequence of baryonic mass expulsion (e.g. Mo & Mao 2004; Mashchenko, Wadsley & Couchman 2008). Alternatively, other effects such as dynamical friction might flatten the very central DM cusp (e.g. Romano-Díaz et al. 2008), which would not affect the overall concentration but could conceivably bias the observational inferences when fitting NFW mass models. However, the low concentrations found by weak lensing could not be ascribed to baryonic effects, so another explanation is needed.

On a related note, it should be remembered that the NFW profile is not a prediction for a real halo even in the absence of baryons, as it represents a composite average of many haloes. Individual haloes would have departures from the NFW density, which might systematically connect to galaxy or group type in a way that creates the appearance of systematic concentration differences (Navarro et al. 2004).

As already mentioned, another possibility is that Fig. 16 reflects selection effects, i.e. the X-ray and GC studies are preferentially picking up systems that have high central DM concentrations (producing unusually high X-ray luminosities and rich GC systems; e.g. Fedeli et al. 2007). Because higher DM densities should arise from halo collapse at earlier times (when the background densities were higher), the implication is that the high-concentration groups collapsed earlier. In order to not contradict the generic expectation of hierarchical structure formation that higher-mass haloes collapse later *on average* (producing trends such as equation 18), the small observed subset of high-concentration systems would come from a high-σ tail of earlier-collapsing high-mass haloes. The different collapse times might also couple with baryonic effects, e.g. adiabatic contraction was stronger at earlier times when the gas content was higher. Such a scenario could be related to suggestions that the slow rotators as a class formed in rapid multiple mergers at higher redshifts, while fast rotators (and presumably late-types) formed at relatively low redshifts, experiencing a small number of isolated major mergers (Burkert, Naab & Johansson 2007).

Thus, there may be a combination of effects in operation: a mass dependency of baryonic, collapse and merger processes in galaxy halo formation, coupled with an observational bias. Whether such a combination could quantitatively explain the observed concentration trends is a question far beyond the scope of this paper, but we do highlight some potential problems.

One issue is the sheer magnitude of the difference between the high- and low-concentration populations. The collapse redshift $z_{\rm c}$ of a DM halo scales roughly with its central density $\rho_{\rm s}$ as $(1 + z_{\rm c}) \propto \rho_{\rm s}^{1/3}$ (e.g. Bullock et al. 2001). The difference between the halo densities on the upper- and lower-concentration sequences is a factor of ∼20, which implies markedly different formation redshifts at the same halo mass. For example, if a typical $10^{13}\,{\rm M}_{\odot}$ halo assembled at $z_{\rm c} \sim 0.9$ (7 Gyr look-back time), then its high-concentration counterpart formed at $z_{\rm c} \sim 4$ (12 Gyr halo age). These haloes would comprise a very small fraction of the total population of the same mass (e.g. Harker et al. 2006), whose presence should be difficult to miss by the dynamical and X-ray observations.

The other problem is that the observed concentrations for the main halo population are too low. Unless there is a vast population of higher-concentration 'dark' galaxy-scale haloes that are still missed by observational surveys, the remaining avenue is alteration of the cosmological parameters. The obvious candidate, σ_8, would have to be lowered substantially to produce the low-concentration trend, perhaps to implausible values (McGaugh et al. 2007). An alternative is to fine-tune the mass dependence of the DM power spectrum (e.g. Alam et al. 2002; McGaugh, Barker & de Blok 2003; Fedeli et al. 2008; Macciò, Dutton & van den Bosch 2008).

The foregoing discussion is a speculative attempt to explain the entire observational picture in the context of the ΛCDM paradigm. However, there is still little direct evidence for ΛCDM halo profiles among all the observational studies of galactic and super-galactic mass distributions; e.g. in NGC 4494, the NFW and LOG potentials fit the data equally well. The possibility remains that the Universe is dominated by an alternative form of DM or of gravity, which might more naturally explain the observations summarized in Fig. 16.

6 CONCLUSIONS

We have presented observations of 255 PNe with line-of-sight velocities in NGC 4494, out to $\sim 7R_{\rm e}$. The basic spatial and kinematical properties of these PNe (including rotation, dispersion and kurtosis) agree well with the field stars, and do not support a distinct origin for the PN progenitors. The mean rotation is low but the system may become rotationally dominated in its outer parts, and we also see evidence for a *kinematically decoupled halo* which may be a

merger signature akin to kinematically decoupled cores. The projected velocity dispersion profile declines with the radius, although not as steeply as in NGC 3379.

We have constructed spherical dynamical models of the system, including a pseudo-inversion Jeans mass model as well as a more standard Jeans analysis using multi-component mass models that include NFW or logarithmic DM haloes, with fourth-order moments being used to constrain the orbital anisotropy. Both approaches give similar results for the mass profile within the radial range constrained by the data. Some DM is required by the data; our best-fitting solution has a radially anisotropic stellar halo, a plausible stellar M/L and a DM halo with a fairly low concentration.

We review the halo parameters determined observationally for other ordinary ETGs such as NGC 4494, as well as for galaxies and groups from the literature. There are preliminary indications that most haloes follow a similar mass–concentration sequence which implies rather low DM densities, accompanied by a population of bright slow-rotator ETGs in group-scale haloes with much higher DM densities. We discuss some possible theoretical scenarios for tying these observations together. Clarifying the situation will require a broad observational survey of galaxies of different types and environments, combined with rigorous dynamical models and improved simulations of galaxy formation. It is the focus of our ongoing PN.S survey (e.g. Coccato et al. 2008) to fill in the critical observational gap of the halo properties of ordinary ETGs. The primary programme includes 12 ellipticals representing a range of sub-types and environments, with an extended survey of 40 early-types in progress, limited only by volume and magnitude.

ACKNOWLEDGMENTS

We would like to thank the Isaac Newton Group staff on La Palma for supporting the PN.S over the years. We thank Gary Mamon for many stimulating discussions on data modelling and comparison with simulations, Ralf Bender, Stacy McGaugh, Thorsten Naab and José Oñorbe for providing their results in tabular form, Mark Wilkinson for further conversations and the referee for constructive comments. NRN has been funded by CORDIS within FP6 with a Marie Curie European Reintegration Grant, contr. n. MERG-FP6-CT-2005-014774, co-funded by INAF. AJR was supported by the National Science Foundation Grant AST-0507729 and by the FONDAP Center for Astrophysics CONICYT 15010003. EOS acknowledges support from NASA through Chandra Award Number AR5-6012X, and thanks Brian McLeod for his assistance with Megacam data reduction. This research has made use of the NED which is operated by the Jet Propulsion Laboratory, California Institute of Technology, under contract with the National Aeronautics and Space Administration. We acknowledge the usage of the HyperLeda data base (http://leda.univ-lyon1.fr).

This work was based on observations made with the William Herschel Telescope operated on the island of La Palma by the Isaac Newton Group in the Spanish Observatorio del Roque de los Muchachos of the Instituto de Astrofisica de Canarias and MMT Observatory, a joint facility of the Smithsonian Institution and the University of Arizona.

REFERENCES

Abadi M. G., Navarro J. F., Steinmetz M., 2006, MNRAS, 365, 747
Aguerri J. A. L., Gerhard O. E., Arnaboldi M., Napolitano N. R., Castro-Rodriguez N., Freeman K. C., 2005, AJ, 129, 2585
Alam S. M. K., Bullock J. S., Weinberg D. H., 2002, ApJ, 572, 34
An J. H., Evans N. W., 2006, AJ, 131, 782
Arnaboldi M. et al., 1996, ApJ, 472, 145
Arnaboldi M., Freeman K. C., Gerhard O., Matthias M., Kudritzki R. P., Méndez R. H., Capaccioli M., Ford H., 1998, ApJ, 507 759
Begeman K. G., Broeils A. H., Sanders R. H., 1991, MNRAS, 249, 523
Bekki K., Peng E. W., 2006, MNRAS, 370, 1737
Bender R., Doebereiner S., Moellenhoff C., 1988, A&AS, 74, 385
Bender R., Saglia R. P., Gerhard O. E., 1994, MNRAS, 269, 785 (B+94)
Bergond G., Zepf S. E., Romanowsky A. J., Sharples R. M., Rhode K. L., 2006, A&A, 448, 155
Bertin E., Arnouts S., 1996, A&AS, 117, 393
Binney J., Mamon G. A., 1982, MNRAS, 200, 361
Binney J., Merrifield, M., 1998, Galactic Astronomy (Galactic Astronomy/James Binney and Michael Merrifield (Princeton Series in Astrophysics). Princeton University Press, Princeton, NJ
Binney J., Tremaine S., 1987, Galactic Dynamics. Princeton University Press, Princeton, NJ, p. 747
Borriello A., Salucci P., Danese L., 2003, MNRAS, 341, 1109
Bosma A., 1981, AJ, 86, 1825
Broadhurst T., Barkana R., 2008, MNRAS, 390, 1647
Broadhurst T., Umetsu K., Medezinski E., Oguri M., Rephaeli Y., 2008, ApJ, 685, L9
Brownstein J. R., Moffat J. W., 2006, ApJ, 636, 721
Bullock J. S., Kolatt T. S., Sigad Y., Somerville R. S., Kravtsov A. V., Klypin A. A., Primack J. R., Dekel A., 2001, MNRAS, 321, 559
Burkert A., 1995, ApJ, 447, L25
Burkert A., Naab T., Johansson P. H., 2008, ApJ, 685, 897
Buzzoni A., Arnaboldi M., Corradi R. L. M., 2006, MNRAS, 368, 877
Capaccioli M., Caon N., D'Onofrio M., 1992, MNRAS, 259, 323
Cappellari M., Emsellem E., 2004, PASP, 116, 138
Cappellari M. et al., 2006, MNRAS, 366, 1126
Cappellari M. et al., 2007, MNRAS, 379, 418 (C+07)
Carollo C. M., Franx M., Illingworth G. D., Forbes D. A., 1997a, ApJ, 481, 710
Carollo C. M., Danziger I. J., Rich R. M., Chen X., 1997b, ApJ, 491, 545
Cattaneo A., Dekel A., Devriendt J., Guiderdoni B., Blaizot J., 2006, MNRAS, 370, 1651
Chanamé J., Kleyna J., van der Marel R., 2008, ApJ, 682, 841
Chiba M., Beers T. C., 2000, AJ, 119, 2843
Ciardullo R., Jacoby G. H., Ford H. C., Neill J. D., 1989a, ApJ, 339, 53
Ciardullo R., Jacoby G. H., Dejonghe H. B., 1993, ApJ, 414, 454
Ciardullo R., Sigurdsson S., Feldmeier J. J., Jacoby G. H., 2005, ApJ, 629, 499
Coccato L. et al., 2008, preprint (arXiv:0811.3203)
Colín P., Klypin A. A., Kravtsov A. V., 2000, ApJ, 539, 561
Comerford J. M., Natarajan P., 2007, MNRAS, 379, 190
Corsini E. M., Wegner G., Saglia R. P., Thomas J., Bender R., Thomas D., 2008, ApJS, 175, 462
Covone G., Paolillo M., Napolitano N. R., Capaccioli M. et al., 2008, ApJ, in press (arXiv:0809.4125)
de Blok W. J. G., McGaugh S. S., Rubin V. C., 2001, AJ, 122, 2396
de Blok W. J. G., Bosma A., McGaugh S., 2003, MNRAS, 340, 657
Dejonghe H., 1986, Physics Reports, 133, 217
Dejonghe H., Merritt D., 1992, ApJ, 391, 531
Dekel A., Stoehr F., Mamon G. A., Cox T. J., Novak G. S., Primack J. R., 2005, Nat, 437, 707 (D+05)
Denicoló G., Terlevich R., Terlevich E., Forbes D. A., Terlevich A., 2005, MNRAS, 358, 813
De Lorenzi F., Gerhard O., Saglia R. P., Sambhus N., Debattista V. P., Pannella M., Méndez R. H., 2008a, MNRAS, 385, 1729 (DL+08a)
De Lorenzi F. et al., 2008b, MNRAS, submitted (arXiv:0804.3350) (DL+08b)
de Vaucouleurs G., de Vaucouleurs A., Corwin H. G. Jr, Buta R. J., Paturel G., Fouque P., 1991, Third Reference Catalogue of Bright Galaxies, Vol. 1, Springer-Verlag, Berlin, Heidelberg, New York, p. 2069
Diaferio A., 1999, MNRAS, 309, 610
Diehl S., Statler T. S., 2007, ApJ, 668, 150

Douglas N. G., Taylor K., 1999, MNRAS, 307, 190
Douglas N. G., Gerssen J., Kuijken K., Merrifield M. R., 2000, MNRAS, 316, 795
Douglas N. G. et al., 2002, PASP, 114, 1234
Douglas N. G., Napolitano N. R., Romanowsky A. J. et al., 2007, ApJ, 664, 257 (D+07)
Duffy A. R., Schaye J., Kay S. T., Dalla Vecchia C., 2008, MNRAS, 390, L64
Dutton A. A., van den Bosch F. C., Dekel A., Courteau S., 2007, ApJ, 654, 27
Emsellem E. et al., 2007, MNRAS, 379, 401
Faber S. M., Wegner G., Burstein D., Davies R. L., Dressler A., Lynden-Bell D., Terlevich R. J., 1989, ApJS, 69, 763
Faber S. M. et al., 1997, AJ, 114, 1771
Fall S. M., Efstathiou G., 1980, MNRAS, 193, 189
Fedeli C., Bartelmann M., Meneghetti M., Moscardini L., 2007, A&A, 473, 715
Fedeli C., Bartelmann M., Meneghetti M., Moscardini L., 2008, A&A, 486, 35
Ferreras I., Saha P., Williams L. L. R., 2005, ApJ, 623, L5
Forestell A., Gebhardt K., 2008, ApJ, submitted (arXiv:0803.3626)
Freeman K. C., 1970, ApJ, 160, 811
Fukazawa Y., Botoya-Nonesa J. G., Pu J., Ohto A., Kawano N., 2006, ApJ, 636, 698
Gao L., Navarro J. F., Cole S., Frenk C. S., White S. D. M., Springel V., Jenkins A., Neto A. F., 2008, MNRAS, 387, 536
Gavazzi R., Treu T., Rhodes J. D., Koopmans L. V. E., Bolton A. S., Burles S., Massey R. J., Moustakas L. A., 2007, ApJ, 667, 176
Gentile G., Salucci P., Klein U., Vergani D., Kalberla P., 2004, MNRAS, 351, 903
Gentile G., Burkert A., Salucci P., Klein U., Walter F., 2005, ApJ, 634, L145
Gentile G., Salucci P., Klein U., Granato G. L., 2007, MNRAS, 375, 199
Gerhard O. E., 1993, MNRAS, 265, 213
Gerhard O., Kronawitter A., Saglia R. P., Bender R., 2001, AJ, 121, 1936
Gilmore G., Wilkinson M. I., Wyse R. F. G., Kleyna J. T., Koch A., Evans N. W., Grebel E. K., 2007, ApJ, 663, 948
Gnedin O. Y., Kravtsov A. V., Klypin A. A., Nagai D., 2004, ApJ, 616, 16
Gnedin O. Y., Weinberg D. H., Pizagno J., Prada F., Rix H.-W., 2007, ApJ, 671, 1115
Goudfrooij P., Hansen L., Jorgensen H. E., Norgaard-Nielsen H. U., de Jong T., van den Hoek L. B., 1994, A&AS, 104, 179 (G+94)
Halliday C., Davies R. L., Kuntschner H., Birkinshaw M., Bender R., Saglia R. P., Baggley G., 2001, MNRAS, 326, 473
Harker G., Cole S., Helly J., Frenk C., Jenkins A., 2006, MNRAS, 367, 1039
Hennawi J. F., Dalal N., Bode P., Ostriker J. P., 2007, ApJ, 654, 714
Henon M., 1973, A&A, 24, 229
Hernquist L., 1990, ApJ, 356, 359
Hinshaw G. et al., 2008, ApJS, submitted (arXiv:0803.0732)
Hui X., Ford H. C., Freeman K. C., Dopita M. A., 1995, ApJ, 449, 592
Humphrey P. J., Buote D. A., Gastaldello F., Zappacosta L., Bullock J. S., Brighenti F., Mathews W. G., 2006, ApJ, 646, 899
Jacoby G. H., 1989, ApJ, 339, 39
Jacoby G. H., Ciardullo R., Harris W. E., 1996, ApJ, 462, 1 (J+06)
Jarrett T. H., Chester T., Cutri R., Schneider S. E., Huchra J. P., 2003, AJ, 125, 525
Jensen J. B., Tonry J. L., Barris B. J., Thompson R. I., Liu M. C., Rieke M. J., Ajhar E. A., Blakeslee J. P., 2003, ApJ, 583, 712
Joanes D. N., Gill C. A., 1998, The Statistician, 47, 183
Kassin S. A., de Jong R. S., Weiner B. J., 2006, ApJ, 643, 804
Kronawitter A., Saglia R. P., Gerhard O., Bender R., 2000, A&AS, 144, 53
Kuzio de Naray R., McGaugh S. S., de Blok W. J. G., 2008, ApJ, 676, 920
Lauer T. R. et al., 2005, AJ, 129, 2138
Lauer T. R. et al., 2007, ApJ, 664, 226
Łokas E. L., 2002, MNRAS, 333, 697
Łokas E. L., Mamon G. A., 2003, MNRAS, 343, 401
Macciò A. V., Dutton A. A., van den Bosch F. C., 2008, MNRAS, in press (arXiv:0805.1926)
Magorrian J., Ballantyne D., 2001, MNRAS, 322, 702
Mamon G. A., Łokas E. L., 2005, MNRAS, 363, 705 (MŁ05)
Mandelbaum R., Seljak U., Kauffmann G., Hirata C. M., Brinkmann J., 2006, MNRAS, 368, 715
Mandelbaum R., Seljak U., Hirata C. M., 2008, Journal of Cosmology and Astro-Particle Physics, 8, 6
Marinoni C., Hudson M. J., 2002, ApJ, 569, 101
Mashchenko S., Wadsley J., Couchman H. M. P., 2008, Sci, 319, 174
McGaugh S. S., Barker M. K., de Blok W. J. G., 2003, ApJ, 584, 566
McGaugh S. S., de Blok W. J. G., Schombert J. M., Kuzio de Naray R., Kim J. H., 2007, ApJ, 659, 149
McLeod B. A., Conroy M., Gauron T. M., Geary J. C., Ordway M. P., 2000, in Bonner Denton M., ed., Proc. of the International Conference on Scientific Optical Imaging. Further Developments in Scientific Optical Imaging. Georgetown, Grand Canyon on 2–5 December, 1998, Royal Society of Chemistry, Cambridge, p. 11
Méndez R. H., Riffeser A., Kudritzki R.-P., Matthias M., Freeman K. C., Arnaboldi M., Capaccioli M., Gerhard O. E., 2001, ApJ, 563, 135
Merrett H. R. et al., 2003, MNRAS, 346, L62
Merrett H. R. et al., 2006, MNRAS, 369, 120
Merrifield M. R., Kent S. M., 1990, AJ, 99, 1548
Milgrom M., Sanders R. H., 2003, ApJ, 599, L25
Mo H. J., Mao S., 2004, MNRAS, 353, 829
Moore B., Quinn T., Governato F., Stadel J., Lake G., 1999, MNRAS, 310, 1147
Naab T., Johansson P. H., Ostriker J. P., Efstathiou G., 2007, ApJ, 658, 710
Napolitano N. R., Arnaboldi M., Freeman K. C., Capaccioli M., 2001, A&A, 377, 784
Napolitano N. R., Arnaboldi M., Capaccioli M., 2002, A&A, 383, 791
Napolitano N. R. et al., 2005, MNRAS, 357, 691 (N+05)
Napolitano N. R. et al., 2008, Proc. IAU Symp. 244, Dark Galaxies and Lost Baryons, p. 289
Navarro J. F., Frenk C. S., White S. D., 1996, ApJ, 462, 563 (NFW)
Navarro J. F., Frenk C. S., White S. D., 1997, ApJ, 490, 493 (NFW)
Navarro J. F. et al., 2004, MNRAS, 349, 1039
Neto A. F. et al., 2007, MNRAS, 381, 1450
Noordermeer E. et al., 2008, MNRAS, 384, 943
Oñorbe J., Domínguez-Tenreiro R., Sáiz A., Serna A., 2007, MNRAS, 376, 39
Ostriker J. P., Peebles P. J. E., 1973, ApJ, 186, 467
O'Sullivan E., Ponman T. J., 2004, MNRAS, 349, 535
Paolillo M., Fabbiano G., Peres G., Kim D.-W., 2003, ApJ, 586, 850
Paturel G., Petit C., Prugniel P., Theureau G., Rousseau J., Brouty M., Dubois P., Cambrésy L., 2003, A&A, 412, 45
Pellegrini S., Ciotti L., 2006, MNRAS, 370, 1797
Pellegrini S., Baldi A., Kim D. W., Fabbiano G., Soria R., Siemiginowska A., Elvis M., 2007, ApJ, 667, 731
Peng E. W., Ford H. C., Freeman K. C., 2004, ApJ, 602, 685
Persic M., Salucci P., Stel F., 1996, MNRAS, 281, 27
Puzia T. H. et al., 2004, A&A, 415, 123
Rasia E., Tormen G., Moscardini L., 2004, MNRAS, 351, 237
Revnivtsev M., Churazov E., Sazonov S., Forman W., Jones C., 2008, A&A, 490, 37
Richtler T., Schuberth Y., Hilker M., Dirsch B., Bassino L., Romanowsky A. J., 2008, A&A, 478, L23
Romano-Díaz E., Shlosman I., Hoffman Y., Heller C., 2008, ApJ, 685, L105
Romanowsky A. J., Kochanek C. S., 1997, MNRAS, 287, 35
Romanowsky A. J., Kochanek C. S., 2001, ApJ, 553, 722
Romanowsky A. J., Douglas N. G., Arnaboldi M., Kuijken K., Merrifield M. R., Napolitano N. R., Capaccioli M., Freeman K. C., 2003, Sci, 301, 1696 (R+03)
Rubin V. C., Thonnard N., Ford J., W. K., 1978, ApJ, 225, L107
Salucci P., Lapi A., Tonini C., Gentile G., Yegorova I., Klein U., 2007, MNRAS, 378, 41
Salpeter E. E., 1955, ApJ, 121, 161
Sambhus N., Gerhard O., Méndez R. H., 2006, AJ, 131, 837
Samurović S., Danziger I. J., 2005, MNRAS, 363, 769
Sanders R. H., McGaugh S. S., 2002, ARA&A, 40, 263

Sazonov S., Revnivtsev M., Gilfanov M., Churazov E., Sunyaev R., 2006, A&A, 450, 117
Schlegel D. J., Finkbeiner D. P., Davis M., 1998, ApJ, 500, 525
Schuberth Y., Richtler T., Dirsch B., Hilker M., Larsen S. S., Kissler-Patig M., Mebold U., 2006, A&A, 459, 391
Sersic J. L., 1968, Atlas de galaxias australes. Observatorio Astronomico, Cordoba, Argentina
Sluis A. P. N., Williams T. B., 2006, AJ, 131, 2089
Spano M., Marcelin M., Amram P., Carignan C., Epinat B., Hernandez O., 2008, MNRAS, 383, 297
Spitler L. R., Forbes D. A., Strader J., Brodie J. P., Gallagher J. S., 2008, MNRAS, 385, 361
Teodorescu A. M., Méndez R. H., Saglia R. P., Riffeser A., Kudritzki R.-P., Gerhard O. E., Kleyna J., 2005, ApJ, 635, 290
Thomas J., Saglia R. P., Bender R., Thomas D., Gebhardt K., Magorrian J., Corsini E. M., Wegner G., 2007, MNRAS, 382, 657
Tiret O., Combes F., Angus G. W., Famaey B., Zhao H. S., 2007, A&A, 476, L1
Tonry J. L., Dressler A., Blakeslee J. P., Ajhar E. A., Fletcher A. B., Luppino G. A., Metzger M. R., Moore C. B., 2001, ApJ, 546, 681
Trager S. C., Worthey G., Faber S. M., Burstein D., Gonzalez J. J., 1998, ApJS, 116, 1
Trager S. C., Faber S. M., Worthey G., González J. J., 2000, AJ, 120, 165
Tran H. D., Tsvetanov Z., Ford H. C., Davies J., Jaffe W., van den Bosch F. C., Rest A., 2001, AJ, 121, 2928
Valdes F., Gupta R., Rose J. A., Singh H. P., Bell D. J., 2004, ApJS, 152, 251
van den Bosch F. C. et al., 2007, MNRAS, 376, 841
van den Bosch R. C. E., van de Ven G., Verolme E. K., Cappellari M., de Zeeuw P. T., 2008, MNRAS, 385, 647
van der Marel R. P., Franx M., 1993, ApJ, 407, 525
Weijmans A.-M., Krajnović D., van de Ven G., Oosterloo T. A., Morganti R., de Zeeuw P. T., 2008, MNRAS, 383, 1343
Wilkinson M. I., Evans N. W., 1999, MNRAS, 310, 645
Wojtak R., Łokas E. L., Gottlöber S., Mamon G. A., 2005, MNRAS, 361, L1
Worthey G., 1994, ApJS, 95, 107
Xue X. et al., 2008, ApJ, 684, 1143
Zhang Y., Gu Q.-S., Ho L. C., 2008, A&A, 487, 177

APPENDIX A: PHOTOMETRY OF NGC 4494

We have obtained a composite photometric profile of NGC 4494 by combining new Megacam observations, detailed in Section 3.1, with literature data which include *HST*-based observations in the *V* and *I* bands (Lauer et al. 2005), and ground-based CCD observations in *BVI* (G+94). The *HST* data are used inside 4.3 arcsec, then G+94 to 32 arcsec and Megacam outside 32 arcsec. The a_4 isophote shape parameter (Bender et al. 1988) is not available for the *HST* data. A small colour gradient is found between the G+94 and the Megacam data at the outer data points, probably due to the background subtraction.

We derive some global photometric parameters for the galaxy by averaging the radially binned values outside 5 arcsec (the central disc region), and weighted by bin luminosities. Thus, we find $\bar{\ } = 0.162 \pm 0.001$, $\overline{a_4} = 0.16 \pm 0.07$ and $\overline{PA} = -0.^{\circ}9 \pm 0.^{\circ}3$.

APPENDIX B: JEANS EQUATIONS

Here, we present the second- and fourth-moment Jeans equations and projections to velocity dispersion $\sigma_{\rm los}$ and kurtosis $\kappa_{\rm los}$, as needed in Section 4.2.3, and closely following Łokas (2002). It is the first time this particular method has been applied to an elliptical galaxy.

Table A1. Combined *V*-band surface photometry of NGC 4494.

R_m (arcsec)	$\mu_V \pm \Delta\mu_V$ (mag arcsec^{-2})		$a_4 \pm \Delta a_4$ (○)	PA
0.020	13.077 ± 0.000	0.187	-	-
0.041	13.406 ± 0.028	0.187	-	-
0.076	13.920 ± 0.005	0.306	-	-
0.103	14.168 ± 0.025	0.436	-	-
0.138	14.440 ± 0.036	0.429	-	-
0.173	14.666 ± 0.034	0.424	-	-
0.233	14.874 ± 0.024	0.273	-	-
0.295	15.054 ± 0.012	0.144	-	-
0.349	15.170 ± 0.007	0.082	-	-
0.393	15.244 ± 0.008	0.078	-	-
0.437	15.344 ± 0.007	0.076	-	-
0.481	15.385 ± 0.006	0.076	-	-
0.523	15.427 ± 0.005	0.082	-	-
0.533	15.470 ± 0.014	0.113	-	-
0.612	15.577 ± 0.011	0.152	-	-
0.688	15.649 ± 0.007	0.229	-	-
0.796	15.790 ± 0.006	0.254	-	-
0.929	15.952 ± 0.006	0.265	-	-
1.092	16.127 ± 0.005	0.266	-	-
1.291	16.330 ± 0.005	0.259	-	-
1.531	16.537 ± 0.005	0.247	-	-
1.817	16.753 ± 0.004	0.234	-	-
2.146	16.969 ± 0.004	0.228	-	-
2.563	17.210 ± 0.004	0.204	-	-
3.053	17.462 ± 0.003	0.184	-	-
3.649	17.716 ± 0.003	0.158	-	-
4.331	17.953 ± 0.003	0.143	0.54 ± 0.17	7.1 ± 0.3
5.184	18.210 ± 0.003	0.110	0.49 ± 0.26	5.2 ± 0.3
5.703	18.340 ± 0.003	0.129	0.45 ± 0.19	4.8 ± 0.4
6.273	18.470 ± 0.004	0.118	0.24 ± 0.26	4.1 ± 0.3
6.900	18.597 ± 0.004	0.128	0.24 ± 0.29	2.9 ± 0.3
7.590	18.718 ± 0.004	0.133	0.63 ± 0.26	1.9 ± 0.2
8.349	18.830 ± 0.005	0.135	0.24 ± 0.30	0.9 ± 0.2
9.184	18.946 ± 0.004	0.146	0.17 ± 0.17	0.7 ± 0.2
10.103	19.059 ± 0.005	0.152	0.09 ± 0.18	0.8 ± 0.2
11.113	19.170 ± 0.005	0.157	0.37 ± 0.18	0.8 ± 0.2
12.224	19.291 ± 0.006	0.167	0.013 ± 0.14	0.7 ± 0.2
13.447	19.413 ± 0.007	0.168	-0.07 ± 0.13	0.5 ± 0.2
14.791	19.544 ± 0.007	0.170	0.11 ± 0.12	0.2 ± 0.2
16.270	19.678 ± 0.008	0.174	0.03 ± 0.15	0.1 ± 0.1
17.897	19.810 ± 0.009	0.175	0.14 ± 0.13	-0.2 ± 0.1
19.687	19.949 ± 0.011	0.173	0.06 ± 0.10	-0.6 ± 0.1
21.656	20.085 ± 0.012	0.185	0.15 ± 0.11	-1.0 ± 0.1
23.821	20.236 ± 0.014	0.183	0.078 ± 0.09	-1.3 ± 0.2
26.204	20.384 ± 0.016	0.180	0.33 ± 0.09	-1.5 ± 0.2
28.824	20.541 ± 0.018	0.176	0.14 ± 0.11	-1.6 ± 0.2
31.706	20.715 ± 0.021	0.171	0.25 ± 0.10	-1.3 ± 0.2
36.729	21.055 ± 0.024	0.149	0.48 ± 0.08	-0.01 ± 0.3
44.130	21.44 ± 0.03	0.147	0.06 ± 0.06	-3.2 ± 0.2
53.266	21.82 ± 0.05	0.137	0.43 ± 0.11	-4.3 ± 0.4
63.918	22.18 ± 0.07	0.137	1.1 ± 0.11	0.8 ± 0.4
77.203	22.58 ± 0.10	0.126	0.15 ± 0.11	-7.3 ± 0.5
91.818	23.02 ± 0.15	0.141	0.47 ± 0.11	-11.4 ± 0.5
110.18	23.49 ± 0.23	0.141	0.29 ± 0.26	-19.4 ± 1.5
132.22	24.1 ± 0.4	0.141	0.46 ± 0.21	-12.4 ± 1.1
158.66	24.6 ± 0.6	0.141	-1.1 ± 0.3	-9.6 ± 1.2
189.26	25.1 ± 1.0	0.151	-1.3 ± 0.4	2.2 ± 1.5
227.11	25.7 ± 1.7	0.151	-1.1 ± 1.0	2.2 ± 3.7
272.53	26.1 ± 2.5	0.151	-	2.2 ± 8.6

We assume that the system is spherically symmetric and that there are no net streaming motions (e.g. no rotation) so that the odd velocity moments vanish and the different components of the dispersion velocity tensor are $\sigma_r^2 = \overline{v_r^2}$, $\sigma_\theta^2 = \overline{v_\theta^2}$ and $\sigma_\phi^2 = \overline{v_\phi^2}$, with $\sigma_\theta^2 = \sigma_\phi^2$ by symmetry. Under these assumptions, the Jeans equations reduce to the simple radial equation (e.g. Binney & Mamon 1982):

$$\frac{\mathrm{d}}{\mathrm{d}r}\left(j\sigma_r^2\right) + \frac{2\beta}{r} j\sigma_r^2 = -j\frac{\mathrm{d}\Phi}{\mathrm{d}r}\ , \tag{B1}$$

where $j_*(r)$ is the 3D number density distribution of the tracer population (e.g. the stars or PNe) and $\Phi(r)$ is the gravitational potential $GM(r)/r^2$ with G the gravitational constant. In equation (B1), the anisotropy parameter, $\beta \equiv 1 - \sigma_\theta^2/\sigma_r^2$, can be either constant or variable with the radius r. In the first case, the equation is simply written as

$$j_*\sigma_r^2(\beta = \mathrm{const}) = r^{-2\beta}\int_r^\infty r'^{2\beta} j_*\frac{\mathrm{d}\Phi}{\mathrm{d}r'}\,\mathrm{d}r' \tag{B2}$$

under the boundary condition $\sigma_r \to 0$ at $r \to \infty$. In the second case, the general solution is

$$j_*\sigma_r^2 = \int_r^\infty j_*\frac{\mathrm{d}\Phi}{\mathrm{d}r'}\int_{r'}^\infty 2\frac{\beta(r'')}{r''}\mathrm{d}r''\mathrm{d}r' \tag{B3}$$

under the same conditions.

The line-of-sight velocity dispersion is obtained from the 3D velocity dispersion by integrating along the line of sight (Binney & Mamon 1982)

$$\sigma_{\rm los}^2(R) = \frac{2}{I(R)}\int_R^\infty \left(1 - \beta\frac{R^2}{r^2}\right)\frac{j_*\,\sigma_r^2\,r}{\sqrt{r^2 - R^2}}\,\mathrm{d}r\ , \tag{B4}$$

where $I(R)$ is the surface density of the tracer and R is the projected radius. For various simple functional forms for $\beta(r)$ (e.g. β constant), the calculation of $\sigma_{\rm los}$ can be reduced to a one-dimensional numerical integration:

$$\sigma_{\rm los}^2(R) = \frac{2G}{I(R)}\int_R^\infty \frac{K j_* M\mathrm{d}r}{r}, \tag{B5}$$

where $K(r)$ is a special function depending on $\beta(r)$ (see appendix A of MŁ05).

To address the well-known mass-anisotropy degeneracy, we consider higher-order moments of the velocity distribution. For the fourth-order moments, the three distinct components $\overline{v_r^4}$, $\overline{v_\theta^4} = \overline{v_\phi^4}$ and $\overline{v_r^2 v_\theta^2} = \overline{v_r^2 v_\phi^2}$ are related by two higher-order Jeans equations (Merrifield & Kent 1990).

In order to solve these equations, we need additional information about the distribution function. We therefore restrict ourselves here to functions which can be constructed from the energy-dependent distribution function by multiplying it by a function of angular momentum $f(E, L) = f_0(E)\,L^{-2\beta}$ with $\beta = \mathrm{const}$. This is an ansatz widely used (Henon 1973; Dejonghe 1986; Wilkinson & Evans 1999; An & Evans 2006), which has the advantage of being easy to integrate even though it does not allow one to generalize to the case of $\beta = \beta(r)$ for the fourth-order moment.

The two Jeans equations then reduce to one:

$$\frac{\mathrm{d}}{\mathrm{d}r}\left(j_*\overline{v_r^4}\right) + \frac{2\beta}{r} j_*\overline{v_r^4} + 3j_*\sigma_r^2\frac{\mathrm{d}\Phi}{\mathrm{d}r} = 0, \tag{B6}$$

whose solution is

$$j_*\overline{v_r^4} = 3r^{-2\beta}\int_r^\infty r'^{2\beta} j_*\sigma_r^2\frac{\mathrm{d}\Phi}{\mathrm{d}r'}\,\mathrm{d}r' \tag{B7}$$

(Łokas 2002). By projection, we obtain the line-of-sight fourth moment

$$\overline{v_{\rm los}^4}(R) = \frac{2}{I(R)}\int_R^\infty \left(1 - 2\beta\frac{R^2}{r^2} + \frac{\beta(1+\beta)}{2}\frac{R^4}{r^4}\right)\frac{j_*\,\overline{v_r^4}\,r}{\sqrt{r^2 - R^2}}\,\mathrm{d}r, \tag{B8}$$

which we calculate numerically.

The fourth projected moment is used together with $\sigma_{\rm los}^4$ in order to obtain the reduced projected kurtosis:

$$\kappa_{\rm los}(R) = \frac{\overline{v_{\rm los}^4}(R)}{\sigma_{\rm los}^4(R)} - 3, \tag{B9}$$

which takes the value of 0 for a Gaussian distribution. The advantage of using the kurtosis is that it can be easily derived from a discrete radial velocity distribution such as our PN data set (see Section 3.4).

One useful corollary of this formalism is that if $\sigma_{\rm los}$ is observationally constant with the radius R, and one assumes that the anisotropy is constant, then the internal kurtosis $\kappa(r) = 0$, and one can calculate a one-to-one relation between $\kappa_{\rm los}$ and β. Therefore, one can estimate the anisotropy as a direct deprojection of the observations, with no dynamical modelling necessary. This approach is of course not applicable to NGC 4494 with its declining VD profile. For reference, the formulae are the following:

$$\kappa_{\rm los}(R) = 3\ \ \frac{I_0 I_4}{I_2^2} - 1\ \ , \tag{B10}$$

$$I_i \equiv \int_R^\infty \frac{f_i\, j_* r\,\mathrm{d}r}{\sqrt{r^2 - R^2}}, \tag{B11}$$

$$f_i = \begin{cases} 1 & (i = 0)\,, \\ 1 - \beta\dfrac{R^2}{r^2} & (i = 2)\,, \\ 1 - 2\beta\dfrac{R^2}{r^2} + \dfrac{\beta(1+\beta)}{2}\dfrac{R^4}{r^4} & (i = 4). \end{cases} \tag{B12}$$

APPENDIX C: FLATTENED MODEL

Here, we present an alternative model needed for Section 4.3, wherein the galaxy is assumed to be axisymmetric and intrinsically flattened but apparently round because it is seen near face-on. To simplify the analysis, we study the dynamics along the galaxy's *observed minor axis only*, where the motions in the galaxy's equatorial angular direction ϕ do not contribute to the observed line-of-sight velocity dispersion $\sigma_{\rm los}$.

Our starting point for the Jeans analysis is an approximate relation between the vertical velocity dispersion and potential in a flattened galaxy:

$$\sigma_Z^2(R, Z) = \frac{1}{j_*}\int_Z^\infty j_*\frac{\partial\Phi}{\partial Z}\,\mathrm{d}Z, \tag{C1}$$

where R is the equatorial radius and Z is the vertical height in the galaxy's reference frame (cf. Binney & Tremaine 1987, equations 4–36). Since we are observing along the minor axis, we will not be concerned with the azimuthal dispersion σ_ϕ, while for the radial dispersion σ_R we adopt an anisotropy parametrization: $\beta_{RZ} \equiv 1 - \sigma_Z^2/\sigma_R^2$.

The local contribution to the dispersion along the line-of-sight z is

$$\sigma_z^2 = \sigma_R^2\ \sin^2 i\ \sin^2\phi + \sigma_\phi^2\ \sin^2 i\ \cos^2\phi + \sigma_Z^2\ \cos^2 i, \tag{C2}$$

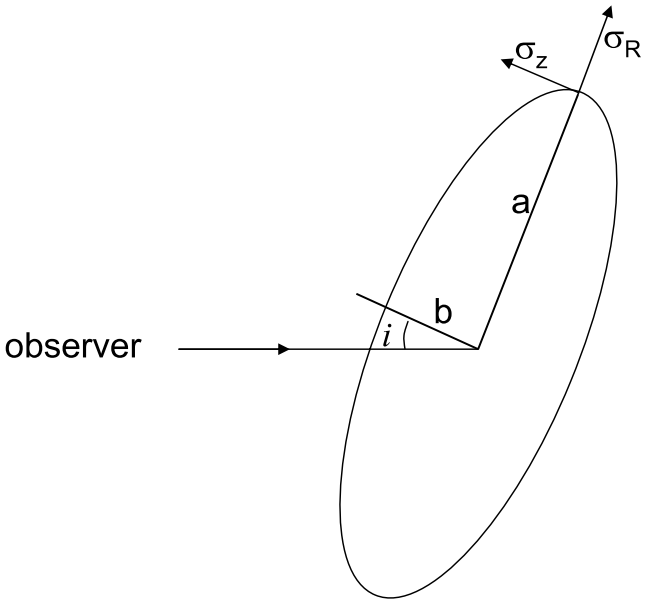

Figure C1. Schematic geometry of the flattened galaxy model, viewed from a line of sight in the plane of the sky. Shown are the inclination i, the intrinsic major- and minor-axis lengths a and b, corresponding to radial and vertical velocity dispersions σ_R and σ_Z. The galaxy is axisymmetric in the equatorial plane (i.e. appears circular when $i = 0^\circ$).

where i is the galaxy's inclination relative to z (see Fig. 17 and cf. Romanowsky & Kochanek 1997 equation 17). Along the minor axis, $\phi = 90^\circ$ and we have

$$\sigma_z^2 = \sigma_R^2 \sin^2 i + \sigma_Z^2 \cos^2 i = \sigma_Z^2 \left(\frac{\sin^2 i}{1 - \beta_{RZ}} + \cos^2 i \right) . \quad \text{(C3)}$$

The observed dispersion in the sky plane (x, y) is then calculated by

$$\sigma_{\rm los}^2(x, y) = \frac{1}{I(x, y)} \int_{-\infty}^{\infty} j_* \sigma_z^2 \mathrm{d}z. \quad \text{(C4)}$$

With a luminosity model $j_*(R, Z)$ and some assumptions for i and β_{RZ}, we now have sufficient equations to link Φ to $\sigma_{\rm los}$.

We derive the intrinsic ellipticity $\varepsilon_{\rm 3D}$ from the observed ellipticity $\varepsilon_{\rm 2D}$ and an assumed inclination i using the following equation:

$$(1 - \varepsilon_{\rm 2D})^2 = (1 - \varepsilon_{\rm 3D})^2 \sin^2 i + \cos^2 i \quad \text{(C5)}$$

(Binney & Merrifield 1998, equation 4.29). For a razor-thin disc ($\varepsilon_{\rm 3D} = 1$), the minimum inclination allowed by the observed flattening of NGC 4494 ($\varepsilon_{\rm 2D} \simeq 0.14$ for $R \gtrsim 0.1\ R_{\rm e}$) is $i = 31^\circ$. More realistically, the most flattened ETGs observed have $\varepsilon_{\rm 2D} \sim 0.75$ (Binney & Merrifield 1998), so as an extreme alternative to the spherical case, we adopt $\varepsilon_{\rm 3D} = 0.75$ ($b/a = 0.25$) and $i = 32^\circ$. For equation (C3), we approximate this to $i = 30^\circ$ and find

$$\sigma_z^2 = \sigma_Z^2 \left(\frac{1}{4(1 - \beta_{RZ})} + \frac{3}{4} \right) . \quad \text{(C6)}$$

We next assume the vertical anisotropy β_{RZ} to be constant throughout the galaxy, and therefore make use of the SAURON dynamical results for galaxies' central regions to make an a priori estimate for β_{RZ}. From C+07 (fig. 7), we find that $\beta_{RZ} \sim 0.5$ is typical for galaxies with the flattening of NGC 4494 ($\varepsilon_{\rm 3D} = 0.75$). From equation (C6), this implies $\sigma_z = 1.1 \times \sigma_Z$, i.e. the line-of-sight dispersion is closely related to the intrinsic vertical dispersion. The anisotropic flattening of the galaxy means σ_Z is relatively low, which is exactly the scenario we are attempting to explore for explaining the low observed values of $\sigma_{\rm los}$. Note also that higher values for β_{RZ} will for the same data imply *lower* intrinsic σ_Z and thus lower mass since the contribution to σ_Z from σ_R will increase.

As a consistency check on our model assumptions, we consider the rotation dominance parameter within $R_{\rm e}$, $(V/\sigma)_{\rm e}$. For the SAURON galaxies, this parameter correlates well with the ellipticity when both parameters are deprojected (C+07, fig. 3). For an NGC 4494 observed value of $(V/\sigma)_{\rm e} \approx 0.26$ (Section 3.2), we search for values of i and β_{RZ} that bring the galaxy into agreement with the correlation (cf. C+07, equation 12). We find $i \sim 40^\circ$ and $\beta_{RZ} \sim 0.2$ with intrinsic $\varepsilon_{\rm 3D} \sim 0.4$ and $(V/\sigma)_{\rm e} \sim 0.4$, suggesting that the true parameters of NGC 4494 could well be intermediate to the extreme spherical and flattened cases that we are considering. Note also that advanced axisymmetric modelling of the comparable galaxies, NGC 3379 and NGC 4697, found that β_{RZ} increases from $\sim$0.3 in the central regions to $\sim$0.5 in the outer parts (DL+08a; DL+08b).

Next, we follow the same steps as in the spherical case (Section 4.2.3) to explore a series of galaxy+DM mass models and compare them to the data. For $j_*(z)$ in equation (C4), we adopt a Hernquist (1990) profile for simplicity with the approximation that the Hernquist radius is the usual $r_{\rm H} = 0.55\ R_{\rm e}$ and $r = \sqrt{R^2 + (z/q)^2}$, with $q = 0.25$, in order to account for the flattening along the line of sight.

Recall that we are now comparing to $v_{\rm rms}$ data along the minor axis only, with no attempt to fit the kurtosis. The best-fitting DM halo has $\Upsilon_* = 3.9 \Upsilon_{\odot,B}$, $\log M_{\rm DM} = 11.91 \pm 0.20$ (the dark mass), a concentration parameter $c_{\rm d} = 2 \pm 1$ and a total virial ratio $f_{\rm vir} = 8 \pm 5$. The latter is lower than the lowest value obtained for the spherical case. As a comparison, we found $\Upsilon(R_{\rm vir}) = 35$ and $\Upsilon_{B5} = 5 \pm 1$, much lower than the values found in Table 5. We therefore find that a face-on flattened configuration is not sufficient to produce a very massive DM halo solution for NGC 4494.

SUPPORTING INFORMATION

Additional Supporting Information may be found in the online version of this article.

Table 3. Catalogue of PNe in NGC 4494.

Please note: Wiley-Blackwell are not responsible for the content or functionality of any supporting information supplied by the authors. Any queries (other than missing material) should be directed to the corresponding author for the article.

This paper has been typeset from a TEX/LATEX file prepared by the author.